

Geochemical Studies of the Battleship Rock Ignimbrite, Valles Caldera, New Mexico

by

Joshua Lombardo

A Thesis Submitted to the Graduate Faculty of the
Auburn University Department of Geosciences
in Partial Fulfillment of the
Requirements for a
Master of Science Degree in Geology

Auburn, Alabama

August 5, 2023

Keywords: Geochemistry, Volcano, CSD, Geothermometry, EMPA

Copyright 2023 by Joshua Lombardo

Approved by:

Dr. Haibo Zou, Chair, Professor

Dr. David T. King, Jr. Professor

Dr. Ashraf Uddin, Professor

Abstract

Valles Caldera is the third largest active super volcano in the United States. Despite this, it remains a poorly understood volcanic system. Evidence has been presented within the last 5 years that suggests that Valles Caldera's eruptive products were spread much farther than previously accepted, as far as Canada. Therefore, it is imperative that new work is put forth to thoroughly understand the recent eruptive history of the caldera in order to better inform disaster response and planning efforts in affected regions.

Battleship Rock Ignimbrite from the Valles Caldera has been understudied when compared to its sister units, and this study aims to attempt to remedy this by making it the primary focus. In this study, zircon U-series dating by secondary ion mass spectrometry (SIMS), Crystal Size Distribution (CSD) analysis, mineral chemistry by Electron Microprobe Analysis (EMPA), and thin section petrology are utilized to characterize the Battleship Rock Ignimbrite of the East Fork Member eruptive products. Both zircon xenocrysts and phenocrysts are present in the Battleship Rock Ignimbrite. The crystal size distribution graphs show varied (concave-up, linear, and mixed) curves. In addition to these quantitative lines of evidence, signs of magma mixing events are also preserved in its plagioclase morphology and chemical makeups. The results of this study support that Valles Caldera underwent magma mixing that triggered the recent eruptions at 70 ka to form the Battleship Rock Ignimbrite.

Acknowledgements

I would like to express my deepest gratitude to Dr. Haibo Zou, for his wisdom, guidance and feedback throughout this project, and for his insights into how not only to conduct research but all of the often unsung aspects of being a competent scientist and academic. I would like to thank my committee members, Dr. David King and Dr. Ashraf Uddin for their patience and guidance as I worked through many struggles, project-related and otherwise, and for the advice they gave during those times. I would also like to thank the Hargett-Dunston award committee for partially funding this thesis project and allowing me to conduct field research at Valles Caldera for this project.

I would like to thank the entire Geosciences Department, and all of the faculty and colleagues that I came to know during my time here for the support, opportunities and encouragement that were afforded to me. I would especially like to thank Dr. John Fronimos and Dr. David King for the opportunities to teach in their classes during my time here. Doing so helped me build confidence in my ability to lead and present effectively and introduced me to several underclassmen friends I would not have had the chance to meet otherwise.

I would like to thank my friends for sharing countless dinners and board-game nights with me, and for always welcoming me with open arms whenever I needed you. I will miss these nights most of all when I think back to my time here. I am also grateful to my friends back home, who always welcomed me back like I never left.

I am grateful to my family for their support during this time and for allowing me to follow my passions without worry. I am incredibly thankful for your praise, kindness and understanding with me as I completed this project.

Finally, I am incredibly grateful to Vanessa. Her tireless support and kindness are no small part of what got me through these few years. Without her unyielding love, support, and advice through every trial I faced, this achievement would not have been possible.

Table of Contents

Abstract	ii
Acknowledgements	iii
List of Tables	vii
List of Figures	viii
Introduction	1
Geologic History	6
Battleship Rock Geologic History.....	6
Geochemical Trends in Quaternary Eruptive Products.....	7
Previous Research	7
Age Dating and Stratigraphic History.....	7
REE Compositional Profile.....	8
Plagioclase Zonation and Resorption.....	11
Crystal Size Distribution Theory and Application.....	13
CSD Theory.....	13
CSD Fundamental Mathematics.....	14
Legacy Work.....	16
Materials and Methods	16
Thin Section Petrography.....	17
Thin Section Descriptions.....	18
Electron Microprobe Analysis.....	20
Crystal Size Distribution.....	22
Pyroxene Thermobarometry.....	24

Plagioclase Thermometry.....	24
Zircon U-Series Geochronology.....	25
Results.....	26
Electron Microprobe Results.....	26
Crystal Size Distribution Results.....	27
Pyroxene Thermobarometry Results.....	32
Plagioclase Thermometry Results	33
Zircon U-Series Geochronology.....	34
Discussion.....	36
Electron Microprobe.....	36
Crystal Size Distribution.....	36
Zircon Geochronology.....	37
Clinopyroxene and Plagioclase Thermometry.....	38
Conclusions.....	39
References.....	40
Appendix.....	47

List of Tables

TABLE 1. Cartwright (2016) $^{87}\text{Sr}/^{86}\text{Sr}$ Results.....	16
TABLE 2. BSH16 Thin Section Compositional Profiles.....	17
TABLE 3. Oscillatory Zoning Compositions.....	27
TABLE 4. Single Pyroxene P-T Results.....	32
TABLE 5. Sample of Plagioclase Thermometer Results from BSH16-2.....	33
TABLE 6. Sample of Plagioclase Thermometer Results from BSH16-3.....	33
TABLE 7. U-series isotope data for zircons from Battleship Rock Ignimbrite	36

List of Figures

Figure 1. *A simplified map of Valles Caldera showing the age of the rhyolite domes from Spell and Harrison (1993) and Phillips et al. (2007), alongside an inset map representing the cross section of the Jemez lineament and the Rio Grande rift that gave rise to the Jemez volcanic field. Image from Zimmerer et al. (2016)*

Figure 2. *A map highlighting the location of the East Fork Member eruptive products. Codes: BBF = Banco Bonito Flow, BRI = Battleship Rock Ignimbrite, ECPB = El Cajete Pyroclastic Beds. SM = South Mountain. The Yellow line is the outline of the Jemez Volcanic field, and the blue line is the outline of the rim of the caldera. From Wolff and Neukampf (2022).*

Figure 3. *A view of Battleship Rock from a nearby picnic site. This angle shows off the battleship-like profile that gave the formation its name.*

Figure 4. *Location of BSH16 sample site collection, base of the Battleship Rock formation.*

Figure 5. *Varied stratigraphic interpretations of the East Fork Member units. Note: “This study” refers to Wolff et al. (2011). Image from Wolff et al. (2011).*

Figure 6. *Spider diagrams for each of the East Fork Member units with chondrite normalization values from Sun and McDonough (1989). Image from Eichler and Spell (2020).*

Figure 7. Schematic diagram showing how mantle derived magmas and crustal melts can interact to generate resorbed plagioclase. Image modeled after Huppert and Sparks (1988). From Wolff and Gardener (1995).

Figure 8. Resorbed plagioclase grain in BSH16-1. This image is taken in plain polarized light.

Figure 9. A plagioclase grain in BSH16-2 that shows zoned resorption patterns, alongside chemical zoning. This image is taken in crossed polarized light.

Figure 10. A plagioclase grain from BSH16-3 that bears a rim of “clean” plagioclase surrounding a resorbed core. This image is taken in plain polarized light.

Figure 11. Top: Thin section map of BSH16-3 with plagioclase grains outlined in magenta. Bottom: Outlines of plagioclase grains filled in. This allows ImageJ to extract relevant shape data when analysis is performed.

Figure 12. Generalized CSD curves adapted from Marsh (1988). Curve A represents the “typical” CSD for a sample in which nucleation and growth rate behave unperturbed to produce a log-linear relationship. Curve B represents a loss of grains due to fractionation, and curves C and D represent accumulation of grains from an external source.

Figure 13. CSD Diagram for BSH16-1. Note the steep change in slope midway through the graph and large error bars. The harsh slope change is indicative of a mixing event, however the low sample size prevents this from being strong evidence on its own.

Figure 14. *CSD Diagram for BSH16-2. Note the slight concave up nature of the graph. This is indicative of an accumulation of larger crystals, likely from another magma source.*

Figure 15. *CSD Diagram for BSH16-3. Note the nearly linear trend on this graph. This is indicative of a “typical” magma. This slope is also near to the slope of smaller grains in BSH16-1’s CSD Diagram. This suggests that they are from the same source, but BSH16-1 experienced some event to alter the population of larger grains.*

Figure 16. *$^{238}\text{U}/^{232}\text{Th}$ ratio plotted against $^{230}\text{Th}/^{232}\text{Th}$ ratio for zircons, with an equiline in green. The whole rock ratio is plotted in blue for comparison.*

1. Introduction

Valles Caldera is the type locality of a resurgent caldera (Smith and Bailey, 1968; Wolff et al., 2011) located approximately 95 Kilometers North of Albuquerque, New Mexico. Its most recent eruptive episodes formed the East Fork Member of the Valles Rhyolite, which contains the El Cajete pyroclastic beds, Battleship Rock Ignimbrite, and the Banco Bonito Lava Flow (Zimmerer et al, 2016). These Quaternary eruptive products potentially represent a new stage of volcanic activity, as the geochemical characteristics of the eruptive products significantly differ from previous eruptions (Wolff and Gardener, 1995). Specifically, the eruptive products of the East Fork Member are more felsic in composition (a transition from andesite-dominated to dacite-dominated products) than previous eruptions (Wolff and Gardener, 1995; Spell et al. 1993). If the caldera is entering a new volcanic cycle, it is imperative that its volcanic history and eruption conditions be better understood, so that proper precautions can be made in the event of an eruption scenario. In order to contribute to the acquisition of this knowledge, various geochemical analyses will be performed on samples from the Battleship Rock Ignimbrite in order to constrain the eruptive conditions and timing of the late quaternary eruptions of Valles caldera.

To this end, electron microprobe analysis (EMPA) and crystal size distribution (CSD) calculations, and zircon uranium-series isotopes will be employed to better constrain the parameters and timing of the late quaternary eruptions. Electron Microprobe Analysis allows for the study of elemental composition of the specimens, as well as allows for the identification of any elemental zoning that may be present in the mineral grains. If zoning is identified, it can allow for the extrapolation of pre-eruptive conditions (Ubide et al. 2019). Crystal size distribution analysis can further inform pre-eruptive conditions by giving insight into the growth rate and population of grains in a magma. U-series isotopes are used to date the crystallization of young zircons and to

constrain the timing of magmatic events. By combining these analytical methods with existing data, a much clearer picture of the eruptive history of the late quaternary eruptive period, specifically the Battleship Rock Ignimbrite, will be generated.

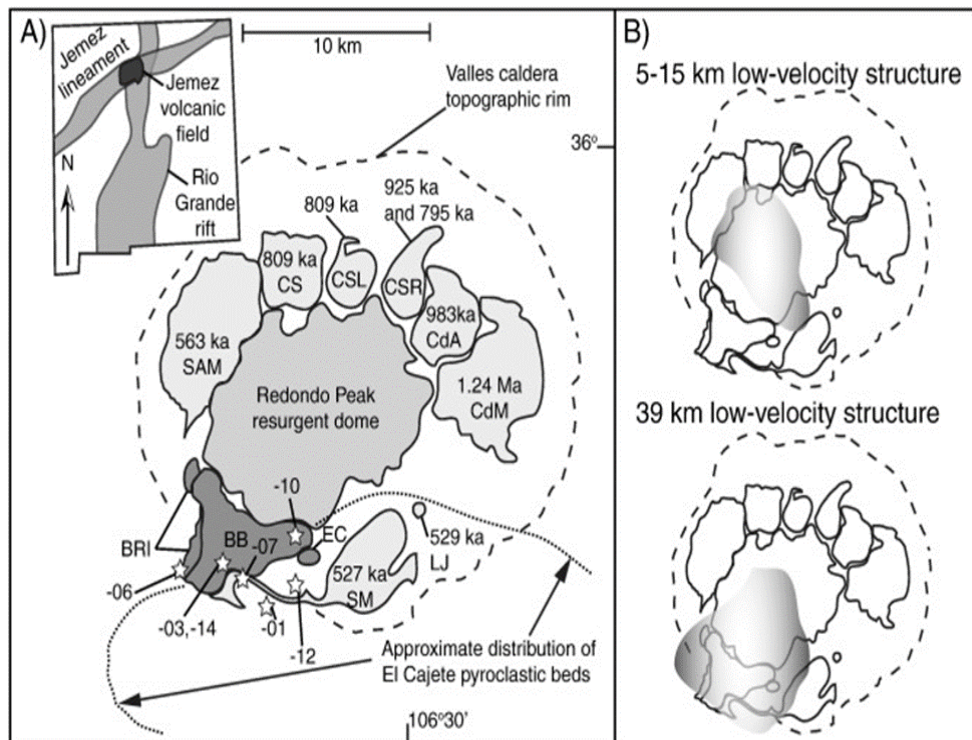


Figure 1. A simplified map of Valles Caldera showing the age of the rhyolite domes from Spell and Harrison (1993) and Phillips et al. (2007), alongside an inset map representing the cross section of the Jemez lineament and the Rio Grande rift that gave rise to the Jemez volcanic field. Image from Zimmerer et al. (2016).

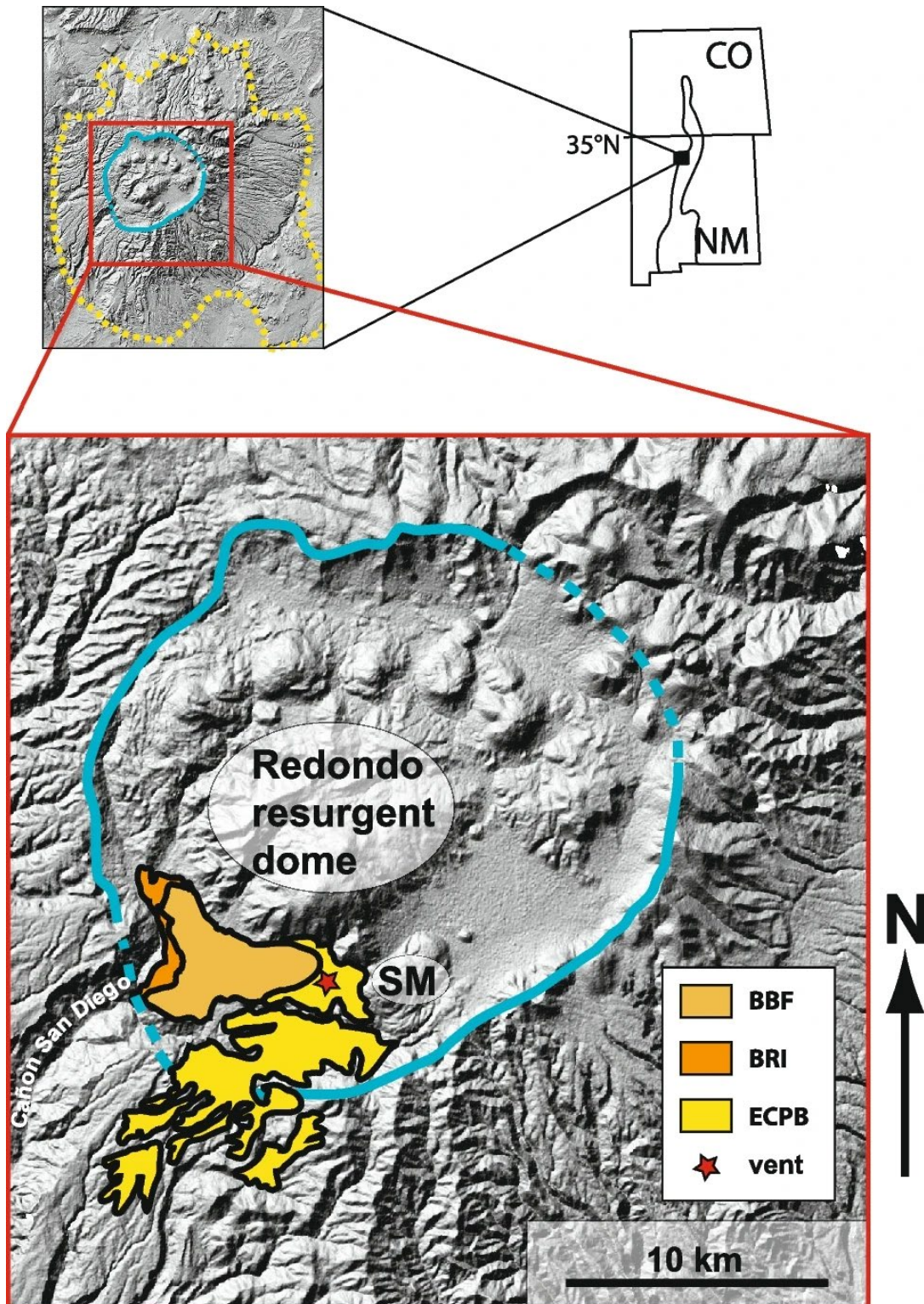


Figure 2. A map highlighting the location of the East Fork Member eruptive products. Codes: BBF = Banco Bonito Flow, BRI = Battleship Rock Ignimbrite, ECPB = El Cajete Pyroclastic Beds. SM = South Mountain. The Yellow line is the outline of the Jemez Volcanic field, and the blue line is the outline of the rim of the caldera. From Wolff and Neukampf (2022).



Figure 3. *A view of Battleship Rock from a nearby picnic site. This angle shows off the battleship-like profile that gave the formation its name.*

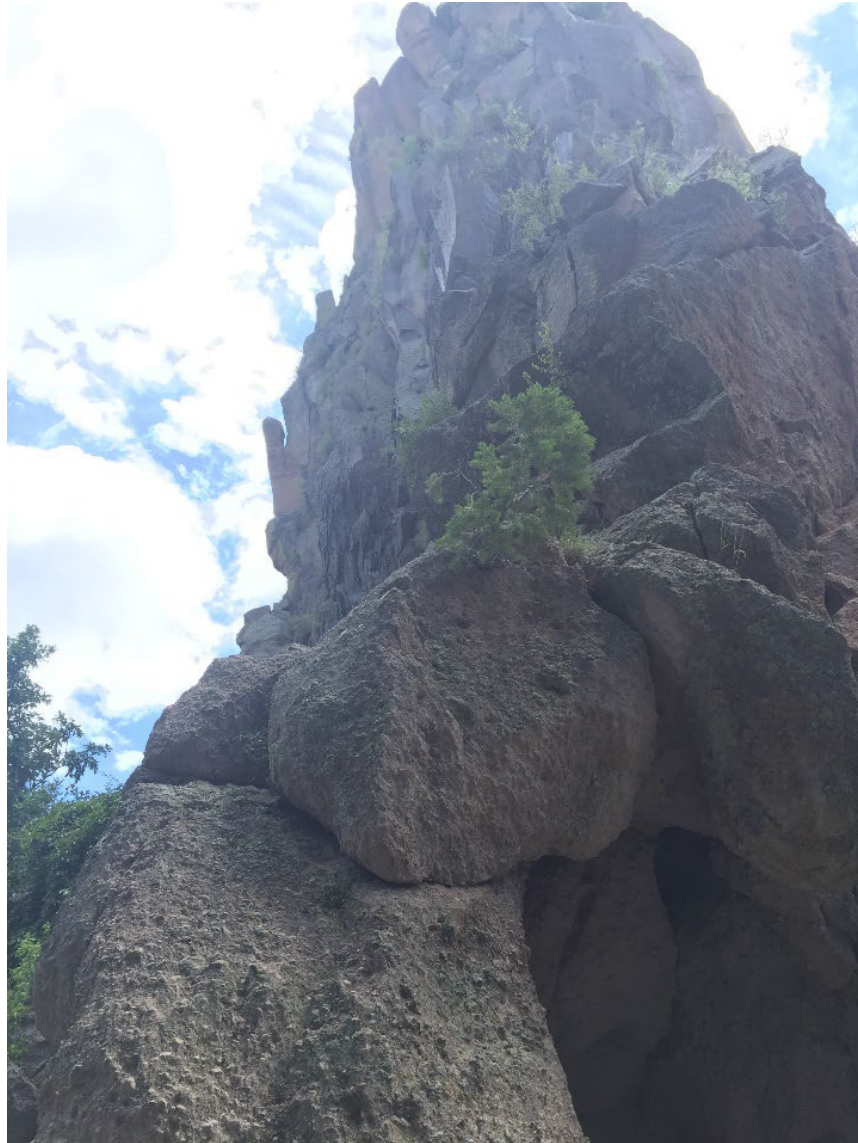


Figure 4. *Location of BSH16 sample site collection, base of the Battleship Rock Ignimbrite formation.*

2. Geologic History

Valles Caldera sits at the cross section of the Jemez Volcanic Field and the Rio Grande rift valley (Dunabr and Hervig 1992). The formation of the Rio Grande Rift began in the late Oligocene, and its expansion created a zone of relatively thin crust (Golombek et al. 1982). This crustal expansion allowed for a multitude of volcanic events to take place, fueled by the Jemez Volcanic Field. At approximately 1.64 Ma, the first major caldera forming eruptive event occurred, creating the Toledo Caldera Complex and depositing the lower Bandelier Tuff member (Otow). Following this, at approximately 1.25 Ma, the Valles Caldera was formed alongside the deposition of the Upper Bandelier Tuff member (Tshirege), and nearly obliterated the Toledo Caldera (Goff et al. 2011). In both cases, there was a significant void space in the upper regions of the magma chamber after the eruption, and the crust that was previously supported by the magma collapsed, creating the caldera (Smith and Bailey 1968; Goff et al. 2011). Post collapse, the renewed magma pressure resulted in the formation of the resurgent dome Redondo Peak, at a relatively rapid pace of only a “few tens of thousands of years” (Goff et al. 2011). Following the formation of the resurgent dome, some comparatively minor eruptions produced the ring of post-caldera domes that partially encircle the northern face of Redondo Peak today (Figure 1). (Goff et al. 2011).

2.1 Battleship Rock Geologic History

Battleship Rock Ignimbrite is an eruptive product of the East Fork Member of the Valles Rhyolite. It is variably welded throughout and was emplaced around 74 ka southwest of the caldera itself (Wolff and Neukampf 2022). As it erupted, it flowed in a southward direction into the Cañon San Diego which served as a mold for the Battleship Rock Ignimbrite to take on its namesake shape (see Figure 3) (Bailey and Smith 1978). McCormick (1989) estimated a cooling temperature

of 500°C based on feldspar xenocrysts for the unit but suggested that this is too low. It was suggested that meteoric water may have had a part in a rapid cooling event, which could explain the low value preserved in the feldspars McCormick (1989).

2.2 Geochemical Trends in Quaternary Eruptive Products

Over the course of the eruptive history of the region, several key compositional trends can be noted. (1) there appears to be a systematic variation in the composition of the Bandelier Tuff from top to bottom. The concentration of silica, quartz, and other constituent materials is higher at the bottom of the tuff (Smith and Bailey 1966), meaning that the upper zone of the magma chamber was more enriched in these materials during this stage of the eruptive cycle. (2) It appears that there has been a larger scale compositional shift between the eruptions that precede the East Fork Member units. More specifically, the East Fork Member units are more felsic in composition than preceding units (Wolff and Gardener, 1995). This led Wolff and Gardener (1995) to speculate that the caldera may be entering a renewed cycle of volcanic activity.

3. Previous Research

3.1 Age Dating and Stratigraphic History

Zimmerer (2016) reported ages for the East Fork Member eruptions using $^{40}\text{Ar}/^{39}\text{Ar}$ and U/Th dating methods. Their methodologies returned an eruption age of 74.4 ± 1.3 ka for El Cajete and Battleship Rock Ignimbrite and 68.3 ± 1.5 ka for Banco Bonito, a significant increase in precision from previously reported ages. Wolff et al. (2011) provided a more detailed reconstruction of the volcanic history for the quaternary eruptions, in which they built upon a previous study by Wolff (1996) and attempts to reconcile some of the varied interpretations

presented by other studies (Bailey et al., 1969; Self et al., 1988; Self et al., 1991; Wolff et al., 1996; Wolff et al., 2011). The variations presented in these interpretations largely center around interpretation of stratigraphy, due to the “imperfect and ephemeral” nature of outcrops among other sources of inconsistency (Wolff et al., 2011). Wolff et al. (2011) provides a series of stratigraphy for the East Fork Members as they are presented in their respective studies (Figure 5). Despite this increase in precision with regard to quaternary events, the overall volcanic system remains poorly understood and documented (Zimmerer et al., 2016). This issue is further highlighted in a 2018 study by Westgate et al. in which a 3m thick ashfall deposit from a Pleistocene era eruption (likely the one that created Valles Caldera) was discovered in Saskatchewan, Canada, over 1000 kilometers outside of the previously accepted extent of eruptive products from this eruption.

3.2 REE Compositional Profile

Eichler and Spell (2020) present chondrite normalized Rare-Earth Element (REE) plots (Spider diagrams) for East Fork Member Rhyolites, which have been reprinted in Figure 6. Each shows a slight negative Europium (Eu) anomaly. Battleship Rock Ignimbrite maintained the lowest concentration of incompatible elements and the highest concentration of compatible elements. REE compositional profiles are reasonably consistent between each of the East Fork Member units.

a

	Bailey et al. (1969)	Self et al. (1988)	Self et al. (1991)	Wolff et al. (1996)	Gardner et al. (2010)	This study
Valles Rhyolite Formation	Banco Bonito Member	Banco Bonito lava flow	Banco Bonito lava flow	Banco Bonito lava flow and ignimbrite	East Fork Member of the Valles Rhyolite (includes the Banco Bonito Flow, Battleship Rock Ignimbrite, VC-1 rhyolite, and El Cajete Pyroclastic Beds)	Banco Bonito Flow
				Banco Bonito ignimbrite		Battleship Rock Ignimbrite (BRI-3)
			VC-1 rhyolite	VC-1 rhyolite		VC-1 Rhyolite
	El Cajete Member	Battleship Rock Ignimbrite, equivalent to or overlying El Cajete pumice deposits	Upper Battleship Rock Ignimbrite	Battleship Rock Ignimbrite, equivalent to upper El Cajete Pumice		Battleship Rock Ignimbrite (BRI-2)
			VC-1 rhyolite			
	Battleship Rock Member	VC-1 tuffs	Lower Battleship Rock Ignimbrite	Lower El Cajete pumice		Battleship Rock Ignimbrite (BRI-1) equivalent to upper El Cajete Pyroclastic Beds
El Cajete pumice deposits			Lower El Cajete Pyroclastic Beds			
Older members of Valles Rhyolite						

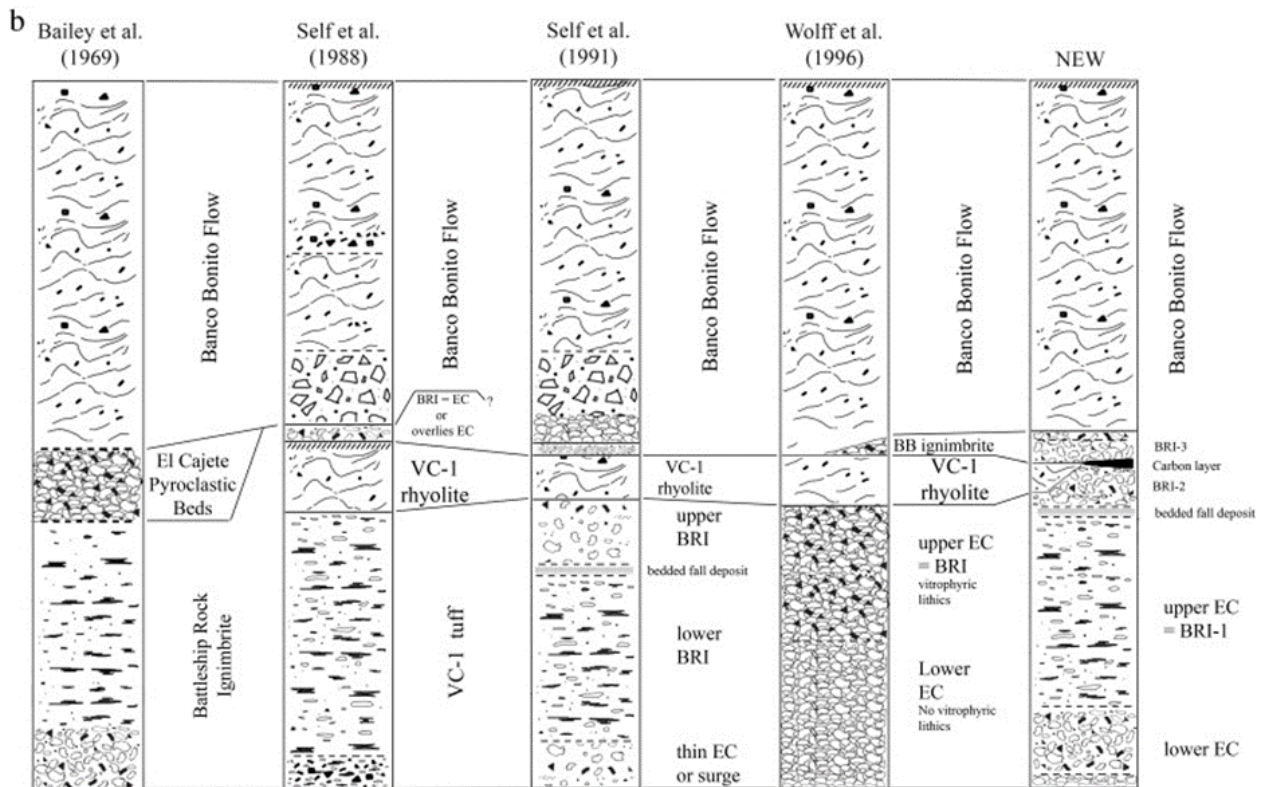


Figure 5. Varied stratigraphic interpretations of the East Fork Member units. Note: “This study” refers to Wolff et al. (2011). Image from Wolff et al. (2011).

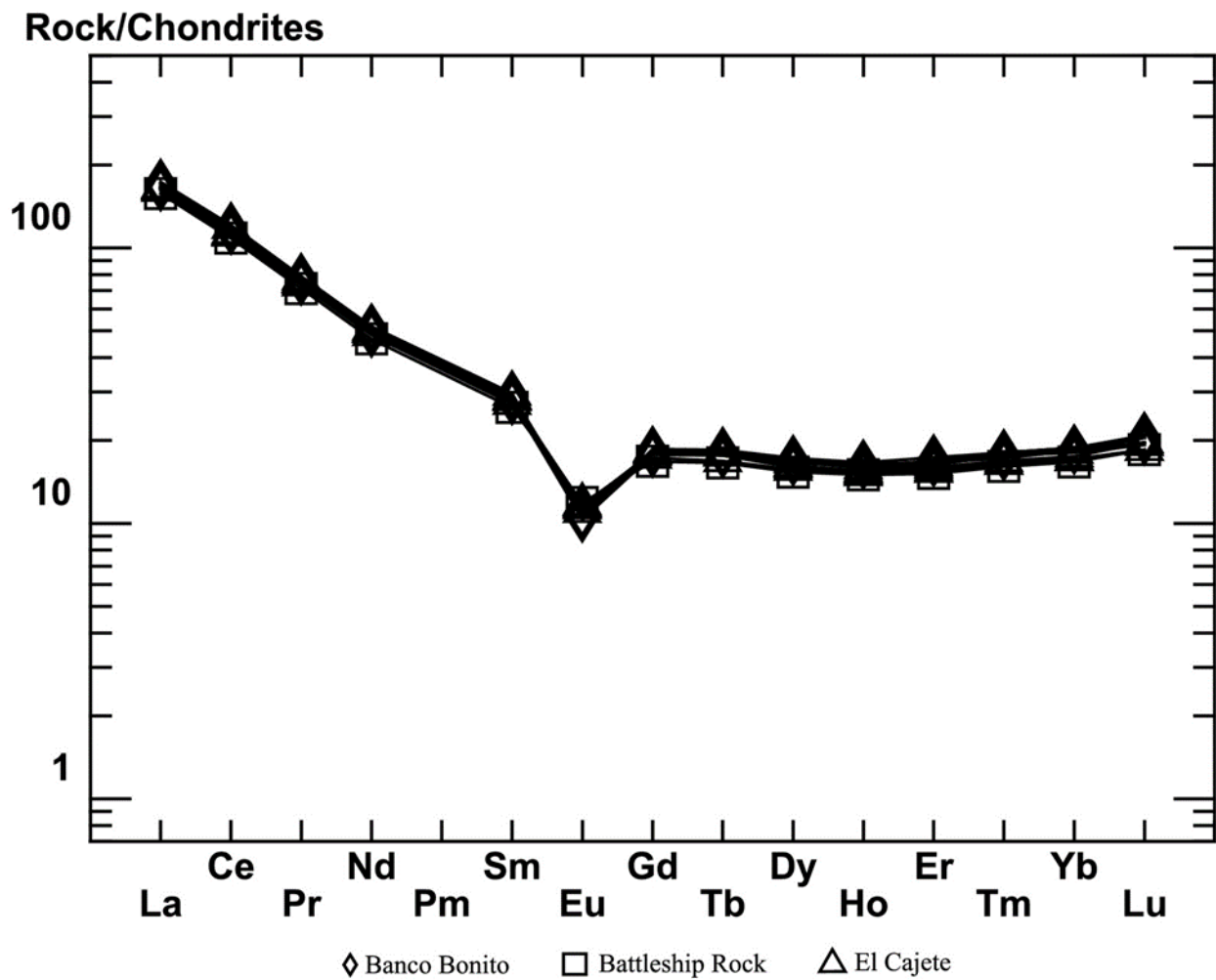


Figure 6. Spider diagrams for each of the East Fork Member units with chondrite normalization values from Sun and McDonough (1989). Image from Eichler and Spell (2020).

3.3 Plagioclase Zonation and Resorption

Zonation of plagioclase has been used as a tool to interpret subsurface magmatic processes and interactions of magmatic events for several magmatic systems (Ikeda 1977; Tepley III et al., 1999; Pietranik et al., 2006; Bennet et al., 2019). Plagioclase is an ideal mineral for this sort of study because it is widespread, crystallizes throughout a magma's history, and is resistant to internal diffusion (Loomis and Welber 1982). Peirce and Kolisnik (1990) presented two categories of compositional zoning. Type I zoning is considered the "typical" zoning and consists of fine (1-10 μm) bands of zonation with compositional variations of 1-10% An. Type II zonation is indicative of some form of disruption in the crystal's growth history and is characterized by much larger zonation bands (up to 100 μm). Magma mixing is one such source of disruption. Loomis and Welber (1982) applied plagioclase zonation-based interpretation techniques to the well-studied Rocky Hill Granodiorite Pluton in order to better quantify how plagioclase reacts to certain changes in the subsurface.

Resorption of plagioclase is another key textural feature to look out for when attempting to uncover a sample's eruptive history. Plagioclase resorption is indicative of mantle recharge (or magma mixing events), as it is a potential product of silicic melt generation, which can occur when a mantle derived magma interacts with a more mature crustal melt (Wolff and Gardener, 1995; Huppert and Sparks, 1988). Resorption effects have been replicated in lab settings (e.g. Tsuchiyama, 1985), therefore the mechanisms that lead to this sieve-like texture are fairly well documented. Tsuchiyama (1985) showed that dissolution of plagioclase into melt can be catalyzed by only a few degrees increase above the equilibrium temperature of a system.

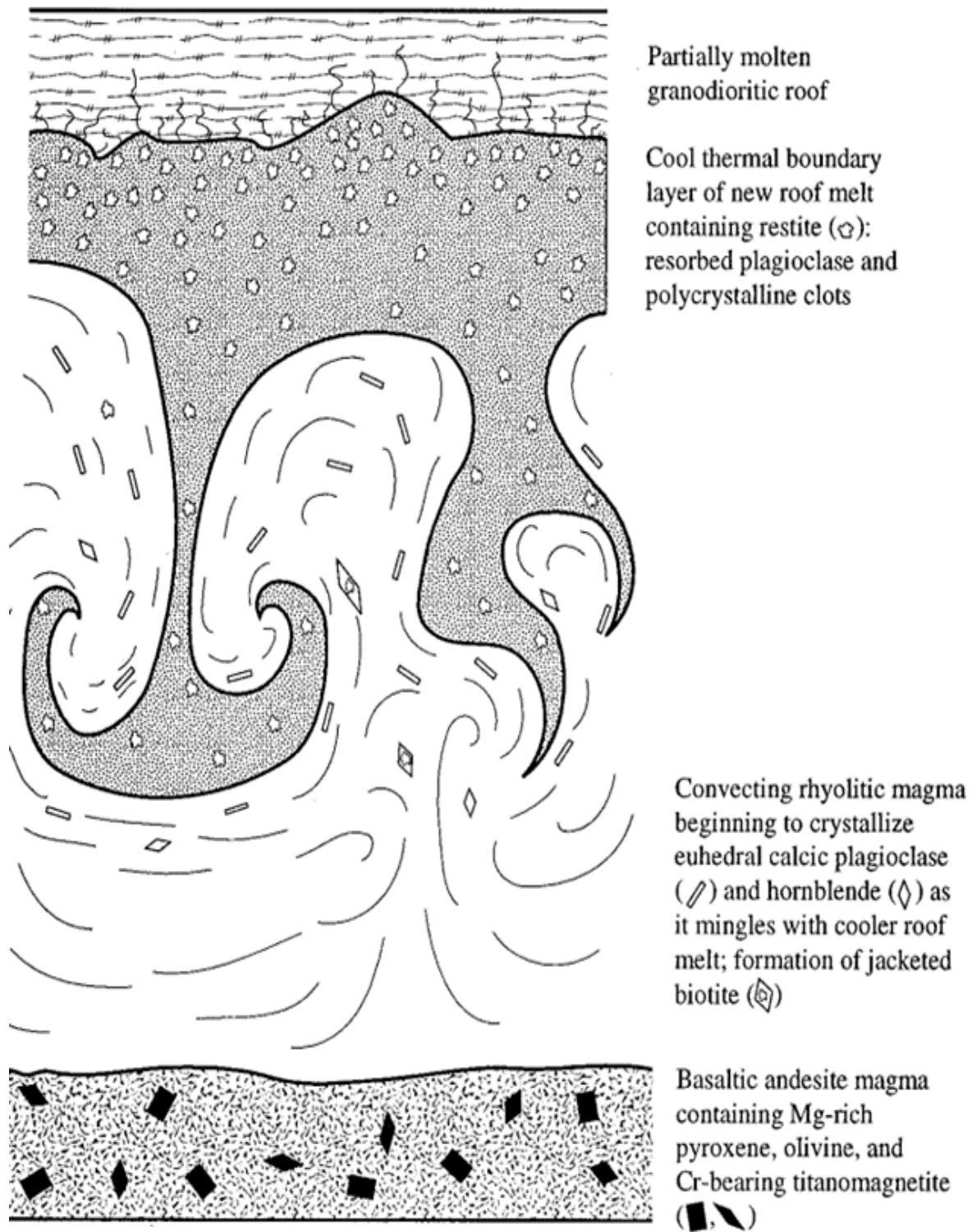


Figure 7. Schematic diagram showing how mantle derived magmas and crustal melts can interact to generate resorbed plagioclase. Image modeled after Huppert and Sparks (1988). From Wolff and Gardener (1995).

3.4 Crystal Size Distribution Theory and Application

Crystal size distribution (CSD) is an analytical technique that aims to take quantitative textural data from a rock sample and utilize it to infer aspects of solidification history (Higgins, 2000). Specifically, CSD analyses attempt to use the size and distribution of a mineral phase in three-dimensional space to accomplish this. This method has been shown to provide more information than mean, modal, or maximum size based analyses (Higgins, 2000).

The use of crystal sizes as a primary point of study in igneous rocks became more accessible due to the publication of seminal papers Marsh (1988) and Cashman and Marsh (1988). These papers reworked the industrial models of Randolph and Larson (1971) into a theoretical basis for CSD application in igneous petrology. Marsh (1988) describes the expected log-linear relationship between population and crystal size groups for a typical magma. Plotting this relationship with the population on the y-axis yields the “CSD diagram” which is the default way to represent this data.

3.4.1 CSD Theory

This section is largely a summary of relevant information excerpted from *Quantitative Textural Measurements in Igneous and Metamorphic Petrology* by Higgins (2006). This book, and the related program developed by Higgins form the foundation of knowledge and application that the CSD work in this study is built upon. Higgins begins his discussion of theory by defining the size of a crystal in this context as a measure of three-dimensional space taken up by a crystal. Growth then, is the change in that size over time. In most geological applications of this idea, growth is a linear change over time.

The primary forces that constrain a crystals growth rate in an igneous setting is the kinetic process of nucleation, which are driven by undercooling and supersaturation of the system. These effects are then coupled with equilibrating effects as the system attempts to reduce its entropy, all the while mechanical deformation could be occurring throughout the system. This leads to a complex three-way interplay between these forces that leave traces of their presence in the resultant textures of the igneous rock. The nucleation rate, or the rate at which new crystals form, is a function of time. The growth rate, however, is a function of time and crystal size. Knowing both functions allows for the change in the CSD over time to be calculated.

3.4.2 CSD Fundamental Mathematics

The intricacies of the CSD methodology have been described in detail in Marsh (1988). It will be heavily abbreviated here to illustrate important concepts but should not serve as a complete breakdown of the underlying mathematics, as they are beyond the scope of this paper. The ultimate goal of CSD analysis is to derive an equation that describes the number of crystals as they nucleate in a liquid or solid environment (Marsh 1988). We begin by making a view declaration about practical components of the model. Firstly, is it necessary to know the populations of crystals present as a function of size, therefore certain allowances must be made in model precision. Due to the nature of how size data must be collected (in the case of this study, by measuring individual grains by hand) it is advantageous to separate sizes into bins (with ranges referred to as ΔL). One might imagine this as different tiers in a sieve, in which a certain size range of grains will be sorted out and trapped. While it is theoretically possible to have sieves with ΔL near 0, this imposes computational challenges, as values within each bin approach 0 if this approach is taken. With that in mind, we begin with the histogram function:

$$N(L) = \int_0^L n(L) dL$$

$N(L)$ is now a function that describes the total number of crystals of size L and smaller. This relationship also implies the following:

$$n(L) = \frac{dN(L)}{dL}$$

$n(L)$ is the population density equation for this system. It also illustrates why having infinitely small sieves (in this case, a dL approaching 0) also reduces $n(L)$ to 0. Now, consider two populations of crystals (n) contained within independent magma bodies of volume V , each with related growth rates (G) and sizes (L) in a range ΔL through a number conservation equation:

$$(V_2 n_2 - V_1 n_1) \Delta L$$

This relationship is controlled by the rate of crystals growing in and out of this ΔL over time interval Δt :

$$(G_1 V_1 n_1 - G_2 V_2 n_2) \Delta t$$

And the influx and outflux of crystals to the system:

$$(Q_i n_i - Q_o n_o) \Delta t \Delta L$$

Which, when combined gives the following equation:

$$(V_2 n_2 - V_1 n_1) \Delta L = (G_1 V_1 n_1 - G_2 V_2 n_2) \Delta t + (Q_i n_i - Q_o n_o) \Delta t \Delta L$$

Simplifying this relationship via division by Δt and ΔL yields:

$$\frac{\partial(Vn)}{\partial t} + \frac{\partial(GVn)}{\partial L} = Q_i n_i - Q_o n_o$$

This equation is the general form of the population balance equation. It can be modified further to fit certain environmental conditions, account for unknowns and so on, which are described in Marsh (1988) on a case-by-case basis.

3.5 Legacy Work

Cartwright (2016) began studying the East Fork Member units through the lens of melt inclusions within samples of the Bandelier Tuff. Specifically, Cartwright (2016) attempted to pair volatile data and $^{87}\text{Sr}/^{86}\text{Sr}$ data collected for melt inclusions of both the Upper and Lower Bandelier Tuff units. The primary volatile contents that were studied were Sulphur (S) and H_2O . Cartwright (2016) found a strong indication of a magma recharge event in the $^{87}\text{Sr}/^{86}\text{Sr}$ data, with a clear negative trend in $^{87}\text{Sr}/^{86}\text{Sr}$ ratio chronologically through the units studied. This indicates an interaction with a lesser evolved magma which may be mantle derived. Mantle injection is widely accepted as a catalyst for explosive felsic eruptions (Folch and Marti, 1998), so Cartwright (2016)'s findings supported further investigation into solidifying this theory.

Table 1. Cartwright (2016) $^{87}\text{Sr}/^{86}\text{Sr}$ Results

Sample	$^{87}\text{Sr}/^{86}\text{Sr}$	Stratigraphic Unit	Relative Age
BDL 3	0.707134 ± 0.000009	Top of Upper Bandelier Tuff	Youngest
BDL 16-11	0.708786 ± 0.000010	Base of Upper Bandeleir Tuff	↑
BDL 16-7	0.709761 ± 0.000009	Base of Lower Bandeleir Tuff	Oldest

4. Materials and Methods

In order to better understand the Valles Caldera volcanic system, several analytical techniques will be performed on samples from the Battleship Rock Ignimbrite. The sample set consists of rhyolites and tuff deposits. Each analysis performed and its purpose are described below.

4.1 Thin Section Petrography

Wagner Petrographic was commissioned to make three petrographic thin sections of the Battleship Rock Ignimbrite (BSH16-1, BSH16-2, and BSH16-3). Each thin section was cut from a different sample of the set. The mineralogical makeup of each thin section is described below.

Table 2. BSH16 Thin Section Compositional Profiles

Minerals	Samples		
	BSH16-1	BSH16-2	BSH16-3
Primary Minerology			
Groundmass	75%	40%	40%
Plagioclase	10%	10%	10%
Biotite	5%	10%	5%
Accessory Minerology			
Quartz	1%	1%	3%
Microcline	-	>1%	-
Hornblende	2%	2%	2%
Oxides	1%	1%	1%
Ilmenite	-	>1%	-
Sanidine	>1%	-	-
Xenocryst Minerology			
Polycrystalline Quartz	-	15%	-
Conglomerate	-	15%	25%
Rhyolite	-	-	15%
Dark Fragments	5%	-	-

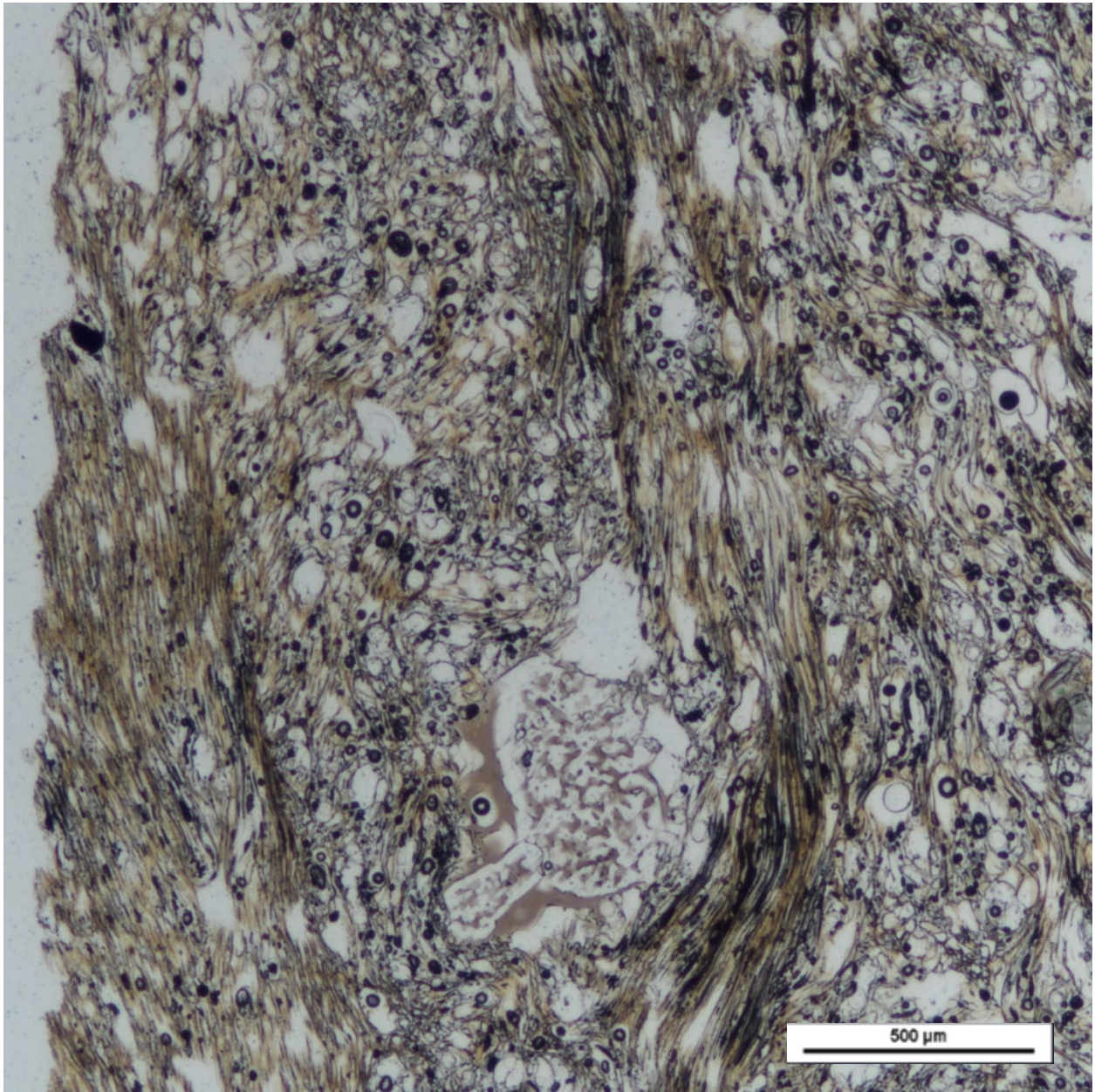


Figure 8. *Resorbed plagioclase grain in BSH16-1. Image is taken in plain polarized light.*

4.1.1 Thin Section Descriptions

BSH16-1. Flow banded groundmass is present throughout much of the sample, the orientation and linearity of which is not consistent throughout. At points, it appears that the flow collects into points of randomly oriented groundmass nodules. The phenocryst assemblage is defined by plagioclase and biotite, with accessory oxides, sanidine, hornblende and quartz. Plagioclase appears as 0.5 to 1 millimeter in diameter anhedral, heavily resorbed grains with characteristic albite twinning. Albite twinning appears to be very sharp in most phenocrysts and very faded in others. Rarely, plagioclase grains can be seen overlying each other. Biotite grains are approximately 1 to 1.5 millimeters in diameter, elongated along the c-axis, and have moderate to high birefringence and high relief. Rarely do grains touch or overlap. Most float isolated in the groundmass, with exception of plagioclase, which can be observed overlying another plagioclase grain, and sanidine, which is observed in a cluster on the edge of the section.

BHS16-2. The BSH16-2 sample primarily contains large xenocryst fragments alongside a primary mineralogy consisting of plagioclase and biotite. Groundmass is primarily light brown to clear in plain polarized light and extinct in crossed polarized light. Plagioclase is anhedral to subhedral 0.5 - 2 millimeter in diameter, clear in plain polarized light, 1st order grays in crossed polars. Fuzzy albite twinning is present in most grains. Almost all grains are heavily resorbed, with a few notable exceptions to this which exhibit stripes of resorption texture alongside clean texture (Figure 9). Relief is moderate. Biotite is euhedral, 0.25-1 millimeter in diameter elongate grains. Green to brown pleochroism in plain polarized light and second order birefringence colors (yellow, green, blue, red) in crossed polarized light. Moderate relief. Most grains have prominent cleavage along

the c-axis. Few grains show bird's eye extinction. Accessory mineralogy consists of quartz, microcline, hornblende, ilmenite and oxides. There are xenocrysts of rhyolite and polycrystalline quartz.

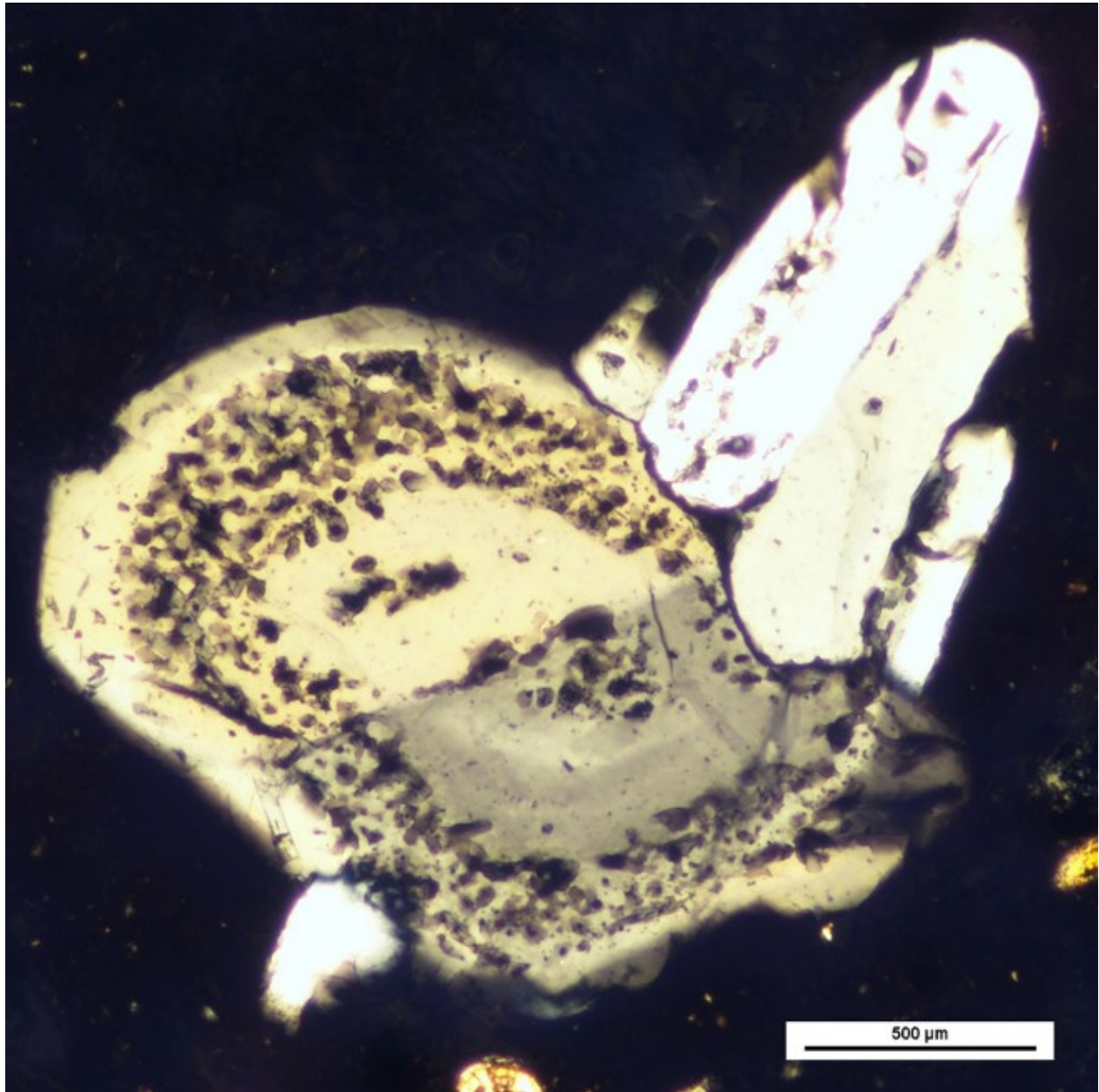


Figure 9. *A plagioclase grain in BSH16-2 that shows zoned resorption patterns, alongside chemical zoning. This image is taken in crossed polarized light.*

BSH16-3. BSH16-3 is identical to BSH16-2 in terms of groundmass, primary and accessory mineralogy, with the exception that BSH16-3 lacks ilmenite. Where the sections differ is in resorption textures and xenocryst content. BSH16-3 has two prominent plagioclase grains that show a rim of clean plagioclase surrounding a heavily resorbed core (Figure 10). Both sections contain rhyolite xenocrysts which bear plagioclase, biotite, hornblende and occasionally quartz. BSH16-3 also bears xenocrysts with significantly darker brown groundmass, and a primary mineral assemblage of quartz. These also appear to have quartz overgrowth rims that vary in thickness along the perimeter of each grain. These rims only appear on the darker (possibly obsidian based) xenocrysts, and not on the rhyolitic xenocrysts.

4.2 Electron Microprobe Analysis

Electron microprobe analysis was conducted at Auburn University's ANIMAL lab on the JEOL JXA-8600 electron microprobe. The three thin sections were loaded into the thin JXA-8600 and spot analysis was conducted on major phenocrysts in each section. The standard used for these analyses was Amelia Albite, and each spot analysis was set up to analyze for the following elements: Si, Ti, Fe²⁺, Mn, Mg, Ca, Na, and K. Primary focus was given to major plagioclase grains to confirm compositional zoning that was identified in microscope observations. Once the spot analysis data was collected, it was analyzed using the MIST (mineral identification by stoichiometry) tool developed by Siebach Lab at Rice University (Siebach, 2022). The MIST tool automatically performs stoichiometric analyses for all of the spot analyses and returns a framework group, species, and mineral formula. 204 spot analyses were conducted, the results of which are printed in Appendix 1.

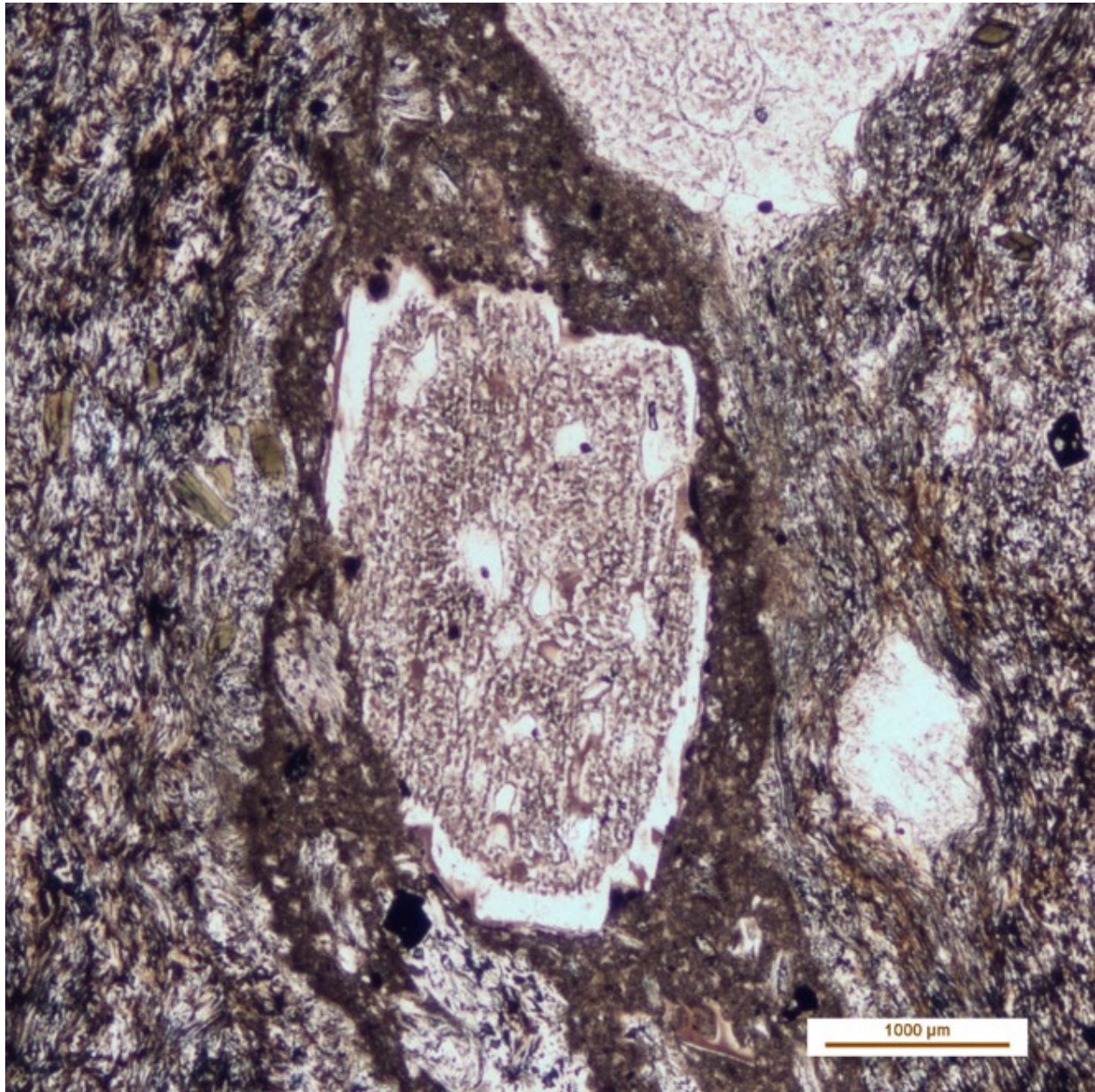


Figure 10. *A plagioclase grain from BSH16-3 that bears a rim of “clean” plagioclase surrounding a resorbed core. This image is taken in plain polarized light.*

4.3 Crystal Size Distribution

Crystal Size Distribution was conducted using a methodology originally developed by Randolph and Larson (1971) for use in chemical engineering and was later expanded upon by several contributors in the field of petrology. This study uses the works of Marsh (1988) and Higgins (1996) as the foundation of its methodology. The procedure is abbreviated as follows.

High-resolution thin section maps (see Appendix 2) were created using a Nikon Eclipse Ci POL Polarizing microscope equipped with a Nikon DS-Ri2 camera. Using the NIS-Elements software, over 200 images were stitched together to create the final map for each section. These images were then exported as .TIF files and loaded into Adobe Illustrator.

In Illustrator, each plagioclase grain was outlined using the pen tool, and the outlines were then loaded into a blank file where they were transformed into solid white shapes in a black field (Figure 11), and the same was done for the outline of the thin section. The vertical extent of the cloud of plagioclase grain shapes was measured and recorded in pixels to serve as a scale factor. Then the files were saved as uncompressed .TIF files and opened in ImageJ.

Following the procedure developed by Higgins, the files were prepped for analysis. Each file was converted to binary from a CMYK image. The scale was set (using the measurements from ImageJ and a physical measurement of the length of the thin section) in millimeters. After this, the files were analyzed, and a table of values was generated. This table was saved as a .CSD file using a macro file developed by Higgins for ImageJ and then opened in CSDCorrections.

In CSDCorrections, estimations of roundness, fabric, and porosity are entered, and then the calculation is run, the output returns a line graph of grain size plotted against population density,

a rose diagram of the grain orientations and a distribution map. Other data is also returned, but these three items are of primary concern to this study.

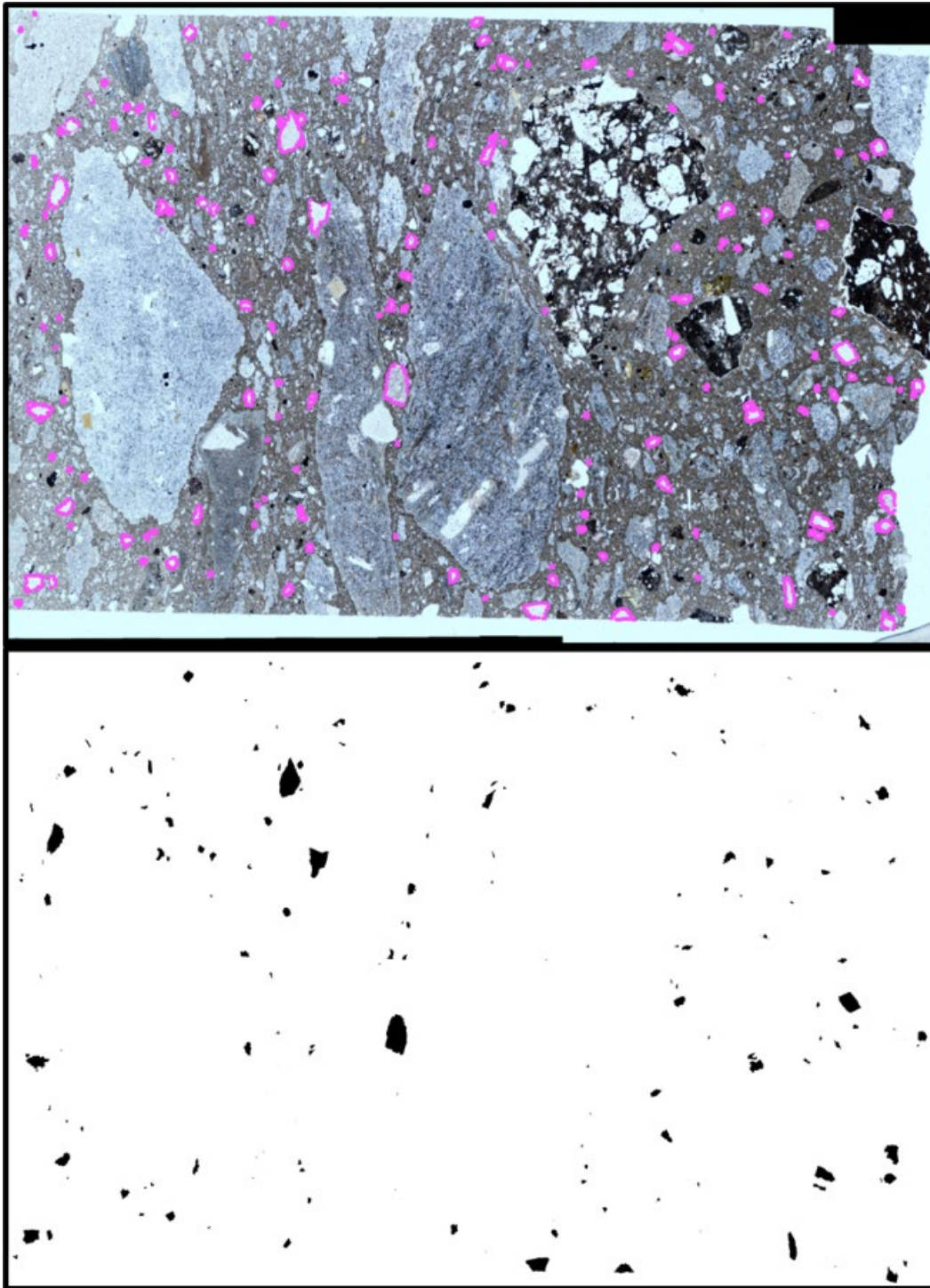


Figure 11. *Top: Thin section map of BSH16-3 with plagioclase grains outlined in magenta. Bottom: Outlines of plagioclase grains filled in. This allows ImageJ to extract relevant shape data when analysis is performed.*

4.4 Pyroxene Thermobarometry

Clinopyroxenes were analyzed with whole rock data in order to ascertain the pre-eruptive pressure and temperature conditions within Valles Caldera at the time of the Battleship Rock Ignimbrite forming eruptions. Single clinopyroxene thermobarometry analysis was conducted using the Excel calculators created by Piturka et al. (2008). This calculator takes in two components, a “liquid composition” which can be the composition of a glass, whole rock, or some other phase that could be in equilibrium with the clinopyroxene, and the clinopyroxene composition itself. Single pyroxene thermobarometry is ideal for analysis of the rhyolites of Valles Caldera because they generally do not contain both orthopyroxene and clinopyroxene in the same sections. The pressures and temperatures are calculated with the following equations:

(1) Pressure Calculation:

$$P(kbar) = -26.27 + 39.16 \frac{T(K)}{10^4} \ln \left(\frac{X_{Jd}^{Cpx}}{X_{NaO_{0.5}}^{liq} X_{AlO_{1.5}}^{liq} (X_{SiO_2}^{liq})^2} \right) - 4.22 \ln(X_{DiHd}^{Cpx})$$

$$+ 78.43 X_{AlO_{1.5}}^{liq} + 393.81 (X_{NaO_{0.5}}^{liq} X_{KO_{0.5}}^{liq})^2$$

(2) Temperature Calculation

$$\frac{10^4}{T(K)} = 7.53 - 0.14 \ln \left(\frac{X_{Jd}^{cpx} X_{CaO}^{liq} X_{Fm}^{liq}}{X_{DiHd}^{cpx} X_{Na}^{liq} X_{Al}^{liq}} \right) + 0.07(H_2O^{liq}) - 14.9(X_{CaO}^{liq} X_{SiO_2}^{liq}) - 0.08 \ln(X_{TiO_2}^{liq})$$

$$- 3.62(X_{NaO_{0.5}}^{liq} + X_{KO_{0.5}}^{liq}) - 1.1(Mg\#^{liq}) - 0.18 \ln(X_{EnFs}^{cps}) - 0.027P(kbar)$$

4.5 Plagioclase Thermometry

For robustness, plagioclase grains were also be used as a thermometer. Plagioclase thermometry was originally introduced by Kudo and Weill (1970) and has received much attention

due to its common occurrence in igneous systems (Piturka, 2008). When conducting this analysis is important to be aware of if the system is expected to be low temperature ($T < 1050$ °C) or high temperature ($T > 1050$ °C) as due to the nature of these models, results may begin to show strong systematic error (Piturka 2008). Plagioclase thermometry will be conducted following the methodology of Piturka (2008) (Equation 23) and the Excel calculator they produced for this purpose. The following equation is the plagioclase-liquid thermometer:

$$\frac{10^4}{T(K)} = 6.12 + 0.257 \ln \left(\frac{X_{An}^{pl}}{X_{CaO}^{liq} (X_{AlO_{1.5}}^{liq})^2 (X_{SiO_2}^{liq})^2} \right) - 3.166(X_{CaO}^{liq}) - 3.137 \left(\frac{X_{AlO_{1.5}}^{liq}}{X_{AlO_{1.5}}^{liq} + X_{SiO_2}^{liq}} \right) + 1.216(X_{Ab}^{pl})^2 - 2.475 \times 10^{-2}(P(kbar)) + 0.2166(H_2O^{liq})$$

4.6 Zircon U-series Geochronology

Zircon SIMS U-series method can date young zircons up to 350 thousand years old (Reid et al., 1997; Reid, 2008). For zircon SIMS U-series surface age analyses (Zou et al., 2010a, 2010b, Schmitt, 2011), individual zircon grains were hand-picked and embedded into soft indium metal to expose the unpolished rims of euhedral zircons (Zou et al., 2021). Immediately prior to analysis, the embedded zircons and their mounts were cleaned using distilled water, 10% HCl, and EDTA solutions to remove any potential surface contamination. Measurements were conducted in a single session using the Stanford-U.S. Geological Survey (USGS) SHRIMP-RG ion microprobe. Analyses followed the analytical protocol, instrumental conditions, and quantification of relative U/Th ionization using Bishop Tuff zircons as described by Vazquez and Lidzbarski (2012) and Marcaida et al. (2019) with raw data reduced with the Squid 2.5

software (Ludwig, 2009). Isochron dates were calculated using the Isoplot 3.75 software (Ludwig, 2012).

5. Results

5.1 Electron Microprobe Results

204 spot analyses were taken between the three BSH16 thin sections, 49 of which were positively identified as plagioclase. Clinoptilolite and heulandite were also identified, suggesting zeolitic alteration. Clinoptilolite was found in abundance growing on the rims and within resorbed spaces of plagioclase grains, and on the rims of amphiboles. Heulandite was found rarely within resorbed spaces of plagioclase.

Plagioclase grains in the BSH16 thin sections showed significant oscillatory and reversed, type II zoning. The oscillatory zoning appears to oscillate between two relatively consistent compositions, which have been averaged and are shown in Table 2 for comparison. Table 3 contains the average compositions of each phase identified in this study, also split by thin section. Two line traverses were conducted to characterize the zonation across plagioclase grains. In these line traverses, clear positive correlations are seen between the relative abundances of Al, Ca and Na. Si, K and Fe also appear to be positively correlated with each other, and this group of elements is negatively correlated to the relative abundances of Al, Ca, and Na. Mg and Mn were present at such low abundances that it is difficult to definitively identify correlation, but they appear to slightly favor positive correlation with Si, K, and Fe. Appendix 1 contains the entire dataset of EMPA data collected and has been separated by thin section. The cores of plagioclase grains in the BSH16 samples vary from sodic compositions to calcic, which is also indicative of a mixed source magma.

Table 3. Oscillatory Zoning Compositions

Oscillatory Zoning Average Compositions		
SiO₂	55.407	69.059
Al₂O₃	25.437	14.631
FeO	0.402	0.970
MnO	0.053	0.164
MgO	0.048	0.233
CaO	8.221	1.653
Na₂O	5.200	3.018
K₂O	0.779	4.554
Total	95.548	94.283

Both baseline amphiboles and calcic amphiboles were identified, with calcic amphiboles more abundant. Calcic amphiboles appeared to be more enriched than baseline amphiboles in all measured elements except Si and Al. Clinoptilolites were found to be potassic in composition, and even the grains that MIST identified as sodic contained only about 0.3% less K than their potassic counterparts. Overall, the compositions between the two groups varied by less than 1% on average, therefore it is safe to classify them together. A few framework silicates compositions were taken, and they on average contained 2.64% - 4.22% K, and 8.97% – 13.44% Al notably.

5.2 Crystal Size Distribution Results

Three CSD graphs were generated and have been printed in Figures 13, 14, and 15. The data sets for each were based on plagioclase grains of each thin section. In total, 39 plagioclase grains were identified in BSH16-1, 111 grains in BSH16-2, and 110 grains in BSH16-3. BSH16-1 had a much lower population of plagioclase grains compared to BSH16-2 and 3. Each graph shows a steeply sloping negative correlation that gently evens out as size increases, which is to be expected. In BSH16-1's case this relationship is slightly more jagged, but that is most likely due to low sample size. Sections also showed little to no favored orientation for plagioclase grains.

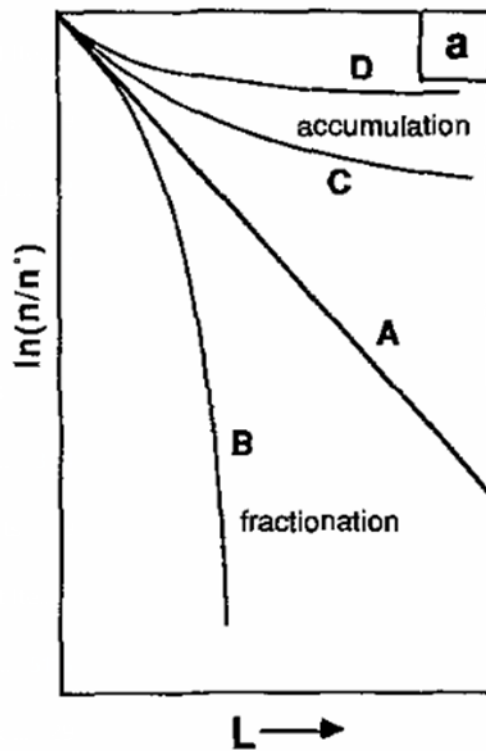


Figure 12. Generalized CSD curves adapted from Marsh (1988). Curve A represents the “typical” CSD for a sample in which nucleation and growth rate behave unperturbed to produce a log-linear relationship. Curve B represents a loss of grains due to fractionation, and curves C and D represents accumulation of grains from an external source.

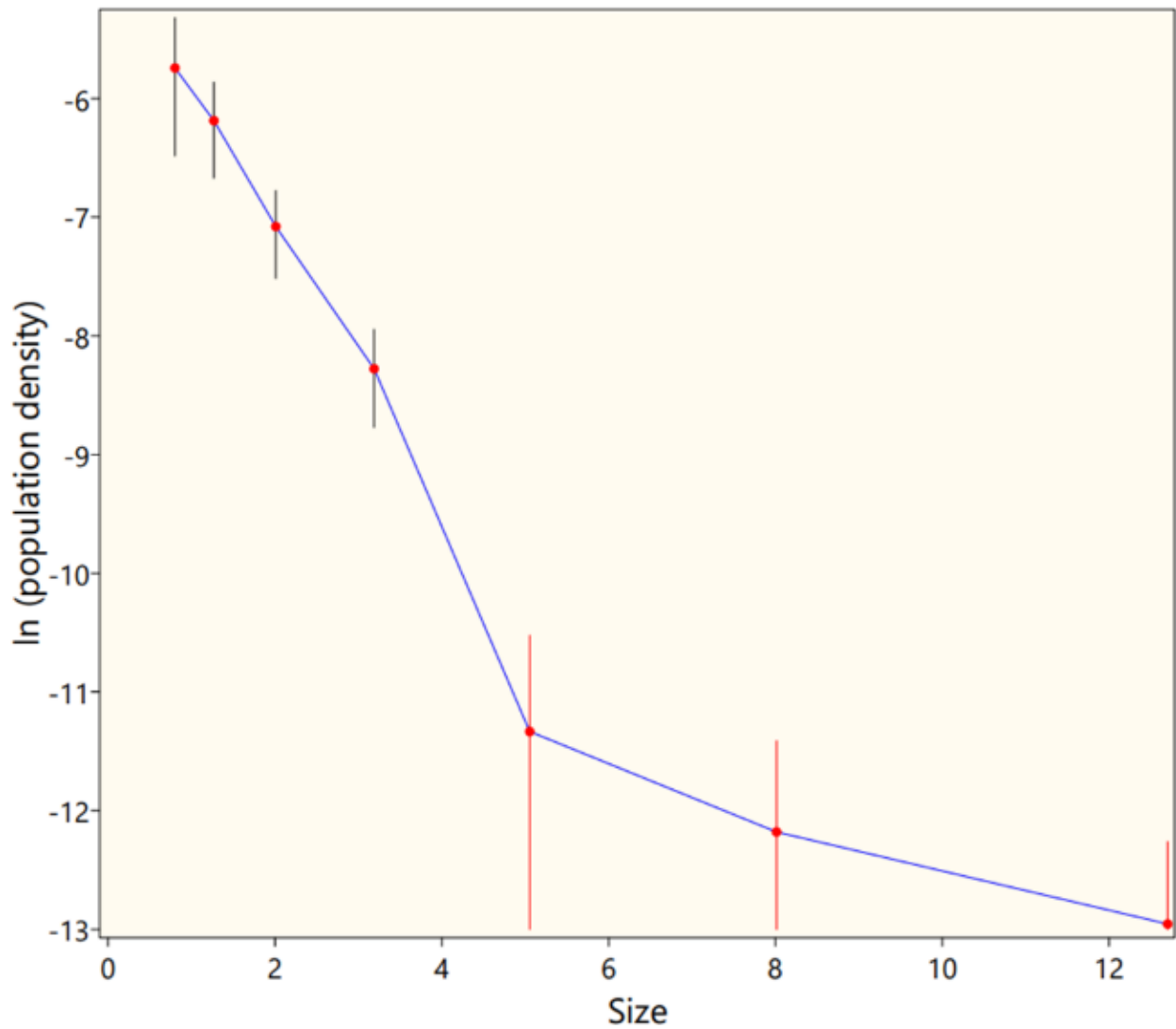


Figure 13. CSD Diagram for BSH16-1. Note the steep change in slope midway through the graph and large error bars. The harsh slope change is indicative of a mixing event, however the low sample size of prevents this from being strong evidence on its own.

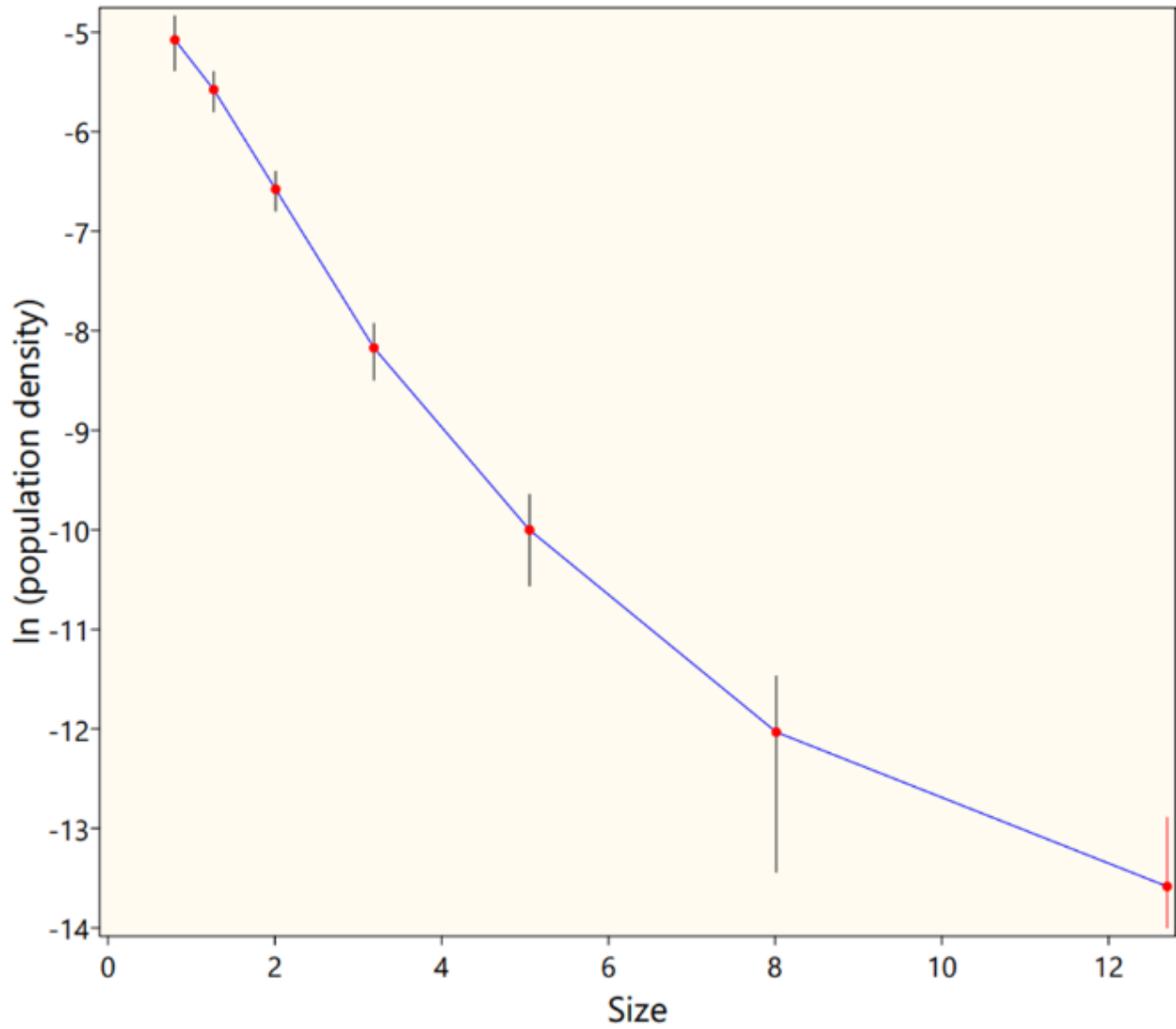


Figure 14. CSD Diagram for BSH16-2. Note the slight concave up nature of the graph. This is indicative of an accumulation of larger crystals, likely from another magma source.

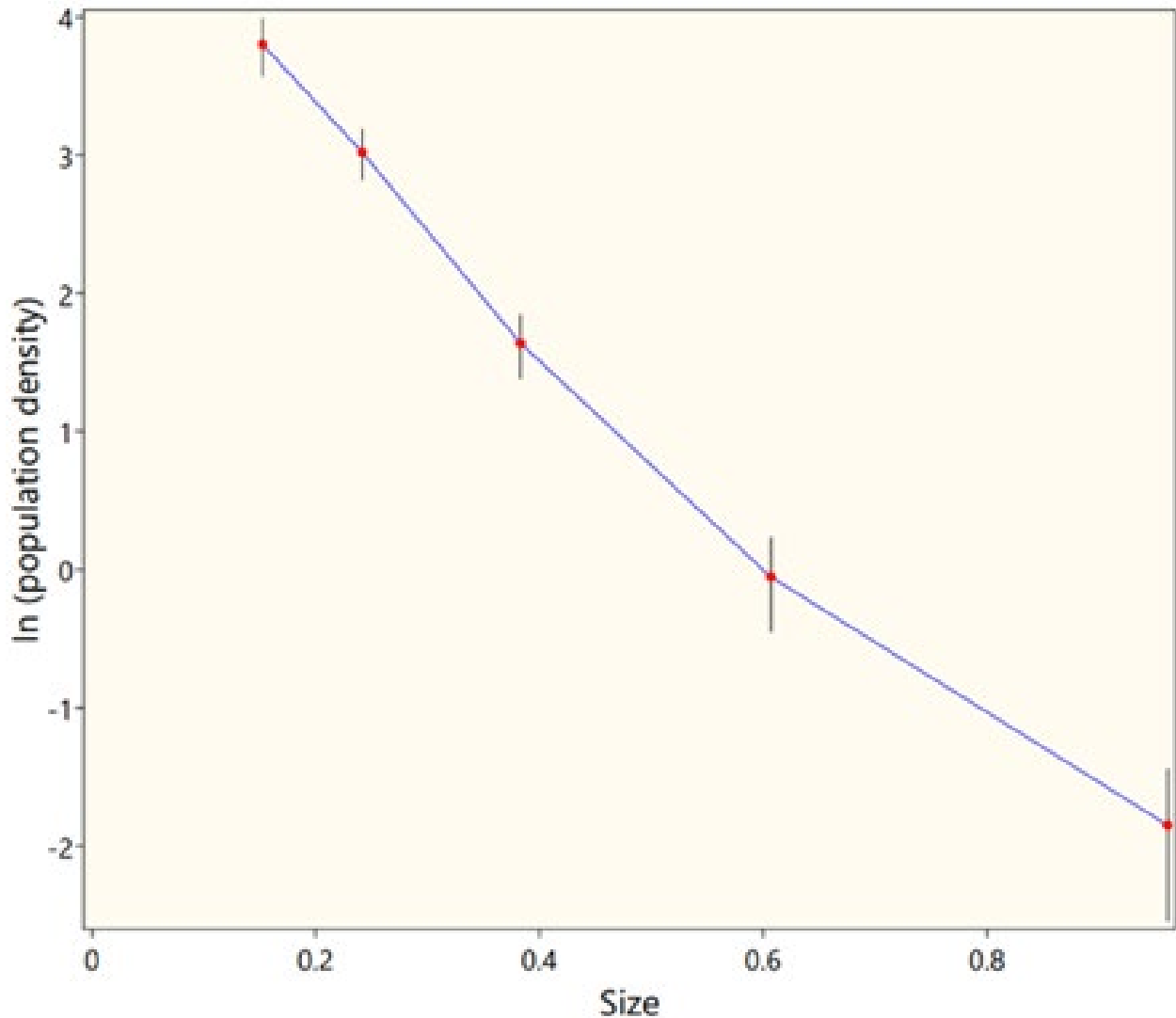


Figure 15. CSD Diagram for BSH16-3. Note the nearly linear trend on this graph. This is indicative of a “typical” magma. This slope is also near to the slope of smaller grains in BSH16-1’s CSD Diagram. This suggests that they are from the same source, but BSH16-1 experienced some event to alter the population of larger grains.

5.3 Pyroxene Thermometry Results

Using whole rock data from Self et al. (1988) and clinopyroxene compositions from the BSH16 samples, pressure and temperature metrics were calculated. The results are printed in Table 4. The clinopyroxenes returned an average temperature of 888 °C, with one significant outlier of 755 °C bringing the average down. Negating this outlier returns an average of 908 °C. The BSH16-1 clinopyroxene grains did not appear to be in equilibrium with the liquid composition and therefore did not return a result in the Piturka (2008) model. This is likely because the clinopyroxenes are xenocrysts. This model did not return K_D values for its calculations.

Table 4. Single Pyroxene P-T Results

Sample	WR (Self et al.)	BSH16-2	BSH16-2	BSH16-3	BSH16-3
SiO ₂	73.28	53.30	52.91	50.54	52.54
TiO ₂	0.29	-	-	-	-
Al ₂ O ₃	13.52	0.76	0.79	0.93	0.55
FeO	2.10	8.70	8.66	7.82	8.03
MnO	0.05	0.32	0.11	0.00	0.00
MgO	0.86	15.89	15.30	15.50	16.06
CaO	1.63	20.05	19.59	19.01	18.05
Na ₂ O	3.99	0.34	0.37	0.28	0.39
K ₂ O	4.19	0.00	0.02	0.06	0.02
Cr ₂ O ₃	0.12	-	-	-	-
P ₂ O ₅	0.08	-	-	-	-
H ₂ O	3.80	-	-	-	-
T (C)		896.2	910.7	903.7	922.9
P (kbar)		7.5	9.2	8.3	9.7

5.4 Plagioclase Thermometry Results

The plagioclase compositions returned a more consistent and higher temperature value when using the Self et al. (1988) whole rock composition as the liquid. The average temperature is 1018 °C. The returned K_D values tended to be high. The expected K_D was 0.25 ± 0.05 for samples returning temperatures below 1050 °C, and the average K_D returned was 0.08. This is likely due to some discrepancy between the whole rock composition and the data collected in this study. A sample of the results from BSH16-2 and BSH16-3 are printed in Tables 5 and 6. The full set of results can be found in Appendix 2.

Table 5. Plagioclase Thermometer Results for Sample BSH16-2

Sample	WR (Self et al.)	BSH16-2									
		1	2	3	4	5	6	7	8	9	10
SiO ₂	73.28	57.21	58.08	57.56	55.42	62.83	61.66	55.59	54.97	64.11	63.07
TiO ₂	0.29	-	-	-	-	-	-	-	-	-	-
Al ₂ O ₃	13.52	27.60	27.74	27.18	27.49	24.78	23.64	28.48	28.70	21.97	23.27
FeO	2.10	0.23	0.21	0.25	0.27	0.27	0.30	0.39	0.37	0.57	0.59
MnO	0.05	0.23	0.00	0.00	0.00	0.99	0.00	0.10	0.18	0.08	0.20
MgO	0.86	0.00	0.01	0.00	0.03	0.02	0.04	0.01	0.06	0.10	0.09
CaO	1.63	8.90	8.87	9.03	9.81	6.82	6.14	10.90	10.76	7.29	6.70
Na ₂ O	3.99	6.17	6.26	5.88	5.09	7.24	7.23	5.46	5.24	4.20	5.71
K ₂ O	4.19	0.42	0.43	0.44	0.39	0.69	0.74	0.32	0.31	2.03	1.34
Cr ₂ O ₃	0.12	-	-	-	-	-	-	-	-	-	-
P ₂ O ₅	0.08	-	-	-	-	-	-	-	-	-	-
H ₂ O	3.80	-	-	-	-	-	-	-	-	-	-
T (C)		1035.8	1035.3	1037.9	1031.2	1013.8	1003.9	1023.0	1023.7	1016.1	999.8
K_D (Ab-An)		0.06	0.06	0.06	0.05	0.09	0.10	0.04	0.04	0.05	0.08

Table 6. Plagioclase Thermometer Results for Sample BSH16-3

Sample	WR (Self et al.)	BSH16-3									
		1	2	3	4	5	6	7	8	9	10
SiO ₂	73.28	63.66	54.75	54.36	54.52	58.94	52.77	54.53	55.32	57.96	54.99
TiO ₂	0.29	-	-	-	-	-	-	-	-	-	-
Al ₂ O ₃	13.52	21.67	27.73	27.84	27.94	23.72	28.67	28.35	28.72	24.57	26.08
FeO	2.10	0.667	0.33	0.291	0.374	0.224	0.515	0.4	0.383	0.275	0.415
MnO	0.05	0.053	0	0	0.051	0	0.026	0.052	0.051	0	0
MgO	0.86	0.153	0.024	0.019	0	0.034	0.064	0.002	0.029	0.053	0.048
CaO	1.63	6.39	10.54	10.11	10.12	6.08	11.13	10.51	9.91	6.36	8.89
Na ₂ O	3.99	4.35	4.86	5.17	4.65	6.48	4.32	4.94	5.01	6.61	5.57
K ₂ O	4.19	2.058	0.399	0.296	0.33	0.767	0.295	0.351	0.387	0.714	0.405
Cr ₂ O ₃	0.12	-	-	-	-	-	-	-	-	-	-
P ₂ O ₅	0.08	-	-	-	-	-	-	-	-	-	-
H ₂ O	3.80	-	-	-	-	-	-	-	-	-	-
T (C)		1056.7	1047.1	1043.6	1034.0	1015.7	1029.2	1025.0	1023.5	987.3	997.6
K_D (Ab-An)		0.06	0.04	0.05	0.04	0.09	0.03	0.04	0.04	0.09	0.06

5.5 Zircon U-series Geochronology

Eight zircon crystals from the welded Battleship Rock Ignimbrite were analyzed for U-Th isotopes by Haibo Zou at the SIMS facility at Stanford University-USGS. The U-series data are provided in Table 7 and plotted on the U-series equiline diagram in Figure 16.

Four zircon grains show ^{238}U - ^{230}Th disequilibrium (Fig. 14) with model ages ranging from 53 ka to 143 ka (Fig. 14). These zircons as phenocrysts have U contents of 50–539 ppm, Th contents of 89–339, and Th/U ratios of 0.63–1.79.

Four other grains plot on the equiline and display U-series equilibrium with ages >350 ka. These zircons as xenocrysts have U contents of 29–436 ppm, Th contents of 14–299, and Th/U ratios of 0.48–0.68. In spite of the limited number of zircon grains for welded ignimbrite, it appears that about 50% of the zircons from the welded Battleship samples are xenocrysts.

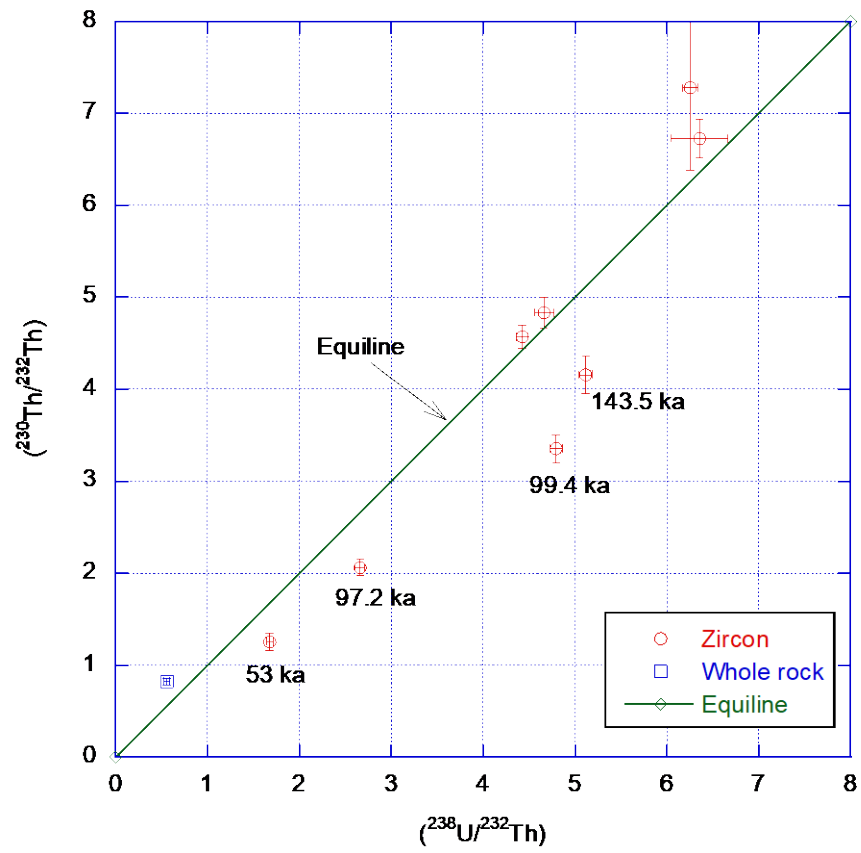


Figure 16. $^{238}\text{U}/^{232}\text{Th}$ ratio plotted against $^{230}\text{Th}/^{232}\text{Th}$ ratio for zircons, with an equiline in green. The whole rock ratio is plotted in blue for comparison.

Table 7. Zircon U-series Isotope Data for Welded Battleship Rock Ignimbrite

Zircons	$(^{238}\text{U}/^{232}\text{Th})$	$(^{230}\text{Th}/^{232}\text{Th})$	Model Age (ka)	+1 sd (ka)
BSHBIG-1.1	6.358	6.726	>350 ka	—
BSHBIG-2.1	4.796	3.353	99.4	10.9
BSHBIG-3.1	4.665	4.832	>350 ka	—
BSHBIG-4.1	2.662	2.060	97.2	14.1
BSHBIG-5.1	5.117	4.155	143.5	20.8
BSHBIG-6.1	6.255	7.277	>350 ka	—
BSHBIG-7.1	4.427	4.569	>350 ka	—
BSHBIG-8.1	1.679	1.251	53.0	17.8
Whole rock*	0.56	0.82		
*Whole rock data from Self et al. (1988)				
sd=standard deviation				

6. Discussion

6.1 Electron Microprobe Analysis

The oscillatory zoning present in the plagioclase grains is strong evidence of fluctuating conditions within the magma chambers of Valles Caldera. If we consider the more calcic phase as the “normal” composition for plagioclase in this melt, the intermittent sodic phases could be evidence for secondary magma intrusion cycles. Silicic melt generation could explain the significant jumps in silica content during these phases, which is triggered during a magma mixing event (Wolff and Gardener, 1995). This may also explain the slight increase in Mg in the plagioclase, as basaltic andesite often carries Mg-rich phases, which may reincorporate during mixing and lend some of their Mg to the newly crystalizing plagioclase phases.

6.2 Crystal Size Distribution

The crystal size density graphs also support the theory that there was potentially one or more magma mixing events. A typical CSD graph for a typical magma should show a log-linear negative correlation between population and grains size (Marsh, 1988). In the BSH16 samples, we

observe relationships that are concave up. There are two reasonable interpretations for these findings, (1) the fractionation of smaller crystals in the portions of the magma chamber that these samples have been taken from served as an input flux for another part of the chamber, or (2) a magma mixing event has occurred, and the resulting CSD graphs are a resultant product of two distinct log-linear CSDs from the two parent magmas. The latter explanation is more convincing for BSH16-1, as the upwards kink in its graph at around size 5 separates two significantly different slopes. BSH16-2 and 3 show a much gentler concave upwards slope, which makes categorizing these as representative of magma mixing events outright more challenging. At this point, there is not enough data from this sample set to draw this conclusion from CSDs alone. However, the fact that the concave upwards relationship was observed is promising. When combined with other evidence presented in this study, the CSD findings support the overall conclusion that a magma mixing event occurred. Future research could solidify this interpretation with the introduction of more CSDs. If other parts of the eruptive products are studied and distinct slopes are discovered that when combined create the CSD shapes observed in BSH16-2 and 3, then there will be strong evidence for a magma mixing event (Marsh 1988).

6.3 Zircon Geochronology

The previous zircon U-series study (Zimmerer et al., 2016) only dealt with unwelded Battleship Rock Ignimbrites. This study focuses on zircons from welded Battleship Rock ignimbrites.

The 53 ± 18 ka phenocrystic zircon age for welded Battleship Rock Ignimbrite reported here is indistinguishable from the 61 ± 5 ka age from unconsolidated Battleship Rock reported by Zimmerer et al. (2016). Two phenocrystic zircons from welded ignimbrite yield a weighted age of

98 ± 17 ka, which is indistinguishable from the 83 ± 7 ka age for the unwelded Battleship Ignimbrite reported by Zimmerer et al. (2016). The phenocrystic zircon age populations for welded Battleship Ignimbrite are similar to those in unwelded Battleship Ignimbrite.

Compared with unwelded ignimbrites, it appears that welded ignimbrites have a higher proportion of xenocrystic zircons. 50% zircons in welded ignimbrites reported here show U-series equilibrium and are xenocrystic zircons. In contrast, none of the 14 zircon crystals display secular equilibrium in unwelded ignimbrite (Zimmerer et al., 2016). Zircon U-series ages reported here for welded Battleship Rock Ignimbrite provide strong evidence for magma mixing or assimilations of the magmas by crustal materials.

6.4 Clinopyroxene and Plagioclase Thermometry

The clinopyroxene results and plagioclase results do not fully agree on a pre-eruptive temperature for the Battleship Rock Ignimbrite forming eruption. This is not a new issue for those working on East Fork Member Units, as there are reported temperatures ranging from approximately 500 °C (McCormick, 1989) to 850 °C (Eichler and Spell, 2020). Although McCormick (1989) did admit that their results were likely the result of rapid cooling and likely not indicative of the true eruption temperature. The pre-eruptive temperature of 850 °C (Eichler and Spell, 2020) was obtained for the Banco Bonito Rhyolite eruption rather than Battleship Rock Ignimbrite eruption.

Our clinopyroxene results suggest an eruption temperature of around 908 °C (when ignoring outliers) and the plagioclase results suggest a pre-eruptive temperature of 1018 °C, a difference of 109 °C. Assuming the Fe-Ti oxide temperature of 850 °C for Banco Bonito Rhyolite of Eichler and Spell (2020) is applicable for the Battleship Rock Ignimbrite, our CPX temperature

of 908 °C is about 50 °C higher than the Fe-Ti oxide temperature, slightly beyond the uncertainty of 30 °C for geothermometers. The even higher plagioclase temperature may suggest earlier crystallization of plagioclase than clinopyroxene. However, there are a number of factors that could be contributing to this discrepancy or uncertainty. The most glaring among these is the lack of published recent whole rock compositional data for Battleship Rock Ignimbrite, and the fact that the whole rock composition of Self et al. (1988) and our samples are likely to be different. Generating whole rock data for the BSH16 samples and re-analyzing the EMPA data in this study against it will likely lead to more accurate results. Additional geothermometers, such as Ti-in-zircon geothermometer (Watson and Harrison, 2005) and Fe-Ti oxide geothermometers (Buddington and Lindsley, 1964), to better constrain the pre-eruptive magma temperatures.

7. Conclusions

The results of this study support the assertion that a magma mixing event has occurred at Valles Caldera. The presence of varied (concave-up, linear and mixed) crystal size distribution graphs suggests magma mixing for the Battleship Rock Ignimbrite. The results of BSH16-2's CSD analysis suggest accumulation and assimilation of new magmatic material that likely catalyzed the eruption of the East Fork Member units. This is further supported by the identification of zircon phenocrysts and xenocrysts by U-series age dating within the welded portions of the Battleship Rock Ignimbrite.

Clinopyroxene and plagioclase thermometry yielded mineral-liquid equilibrium temperatures for the Battleship Rock Ignimbrite. Clinopyroxene thermometry suggested an equilibrium temperature of approximately 900 °C, while plagioclase thermometry suggests an equilibrium temperature of around 1000 °C. This difference in temperatures may indicate the

earlier crystallization of plagioclases than clinopyroxenes. More accurate whole rock data will likely improve these temperature estimates. If either of these estimates are validated for eruptive temperatures through further study, then they suggest that Valles Caldera's Quaternary eruptions of Battleship Rock Ignimbrite unit occurred at a significantly higher temperature than previously thought.

References

- Bailey, R. A. (1969) Stratigraphic nomenclature of volcanic rocks in the Jemez Mountains, New Mexico. *Contributions to Stratigraphy*, Geological Survey Bulletin 1274-P.
- Bennett, E. N., Lissenberg, C.J. & Cashman, K.V. (2019) The significance of plagioclase textures in mid-ocean ridge basalt (Gakkel Ridge, Arctic Ocean). *Contributions to Mineralogy and Petrology* 174: 49.
- Buddington, A. F., Lindsley, D.H. (1964) Iron-titanium oxide minerals and synthetic equivalents. *Journal of Petrology* 5(2): 310-357.
- Cartwright, J. (2016) Volatile and Sr Isotope Analysis of Melt Inclusions from the Bandelier Tuff, Valles Caldera, New Mexico: Insights into Pre-Eruptive Magma Conditions. Masters Thesis, Auburn University
- Cashman, K. V. (1990) Textural constraints on the kinetics of crystallization of igneous rocks. *Reviews in Mineralogy and Geochemistry* 24: 259–314.
- Cashman K.V., Marsh B. D. (1988) Crystal size distribution (CSD) in rocks and the kinetics and dynamics of crystallization II. Makaopuhi lava lake. *Contributions to Mineralogy and Petrology* 99:292–305
- Dunbar, N. W. & Hervig, R. L. (1992) Volatile and trace element composition of melt inclusions from the Lower Bandelier Tuff: Implications for magma chamber processes and eruptive style. *Journal of Geophysical Research* 97 (B11): 15129-15150.
- Eichler, C. M. & Spell, T. L. (2020) Petrogenesis of three East Fork Member rhyolites of the Jemez volcanic field, Valles caldera, New Mexico, USA. *Journal of Volcanology and Geothermal Research* 389: 106706.

- Ellertsdottir, E. T. (2014) Eyafjallajökull and the 2010 Closure of European Airspace: Crisis Management, Economic Impact, and Tackling Future Risks. *Applied Economics* 9, 127-137.
- Folch, A. & Martí, J. (1998) The generation of overpressure in felsic magma chambers by replenishment. *Earth and Planetary Science Letters* 163 (1–4): 301–314.
- Goff, F., Gardner, J. N., Reneau, S. L., Kelly, S. A., Kempton, K. A., & Lawrence, J. R. (2011) *Geologic map of the Valles caldera, Jemez Mountains, New Mexico*. New Mexico Bureau of Geology and Mineral Resources.
- Goff, F., Warren, R. G., Goff, C. J., & Dunbar, N. (2014). Eruption of reverse-zoned upper Tshirege Member, Bandelier Tuff from centralized vents within Valles caldera, New Mexico. *Journal of Volcanology and Geothermal Research* 276: 82–104.
- Golombek, M. P., McGill, G. E. & Brown, L. (1983) Tectonic and geologic evolution of the Espanola Basin, Rio Grande Rift: Structure, rate of extension, and relation to the state of stress in the western United States. *Tectonophysics* 94(1–4): 483–507.
- Higgins, M. (1996) Crystal size distributions and other quantitative textural measurements in lavas and tuff from Egmont volcano (Mt. Taranaki), New Zealand. *Bulletin of Volcanology* 58: 194–204.
- Higgins, M. D. (2000) Measurement of crystal size distributions. *American Mineralogist* 85 (9): 1105–1116.
- Higgins, M. D. (2006) *Quantitative Textural Measurements in Igneous and Metamorphic Petrology* (1st ed.). Cambridge University Press.
- Huppert, H. E. & Sparks, R.S.J. (1988) The Generation of Granitic Magmas by Intrusion of Basalt into Continental Crust. *Journal of Petrology* 29: 599-624.

- Huang, R. & Audétat, A. (2012) The titanium-in-quartz (TitaniQ) thermobarometer: A critical examination and re-calibration. *Geochimica et Cosmochimica Acta* 84: 75–89.
- Ikeda, Y. (1977) Grain size of plagioclase of the basaltic andesite dikes, Iritono, central Abukuma plateau. *Canadian Journal of Earth Sciences* 14(8): 1860-1866.
- Kudo AM & Weill DF (1970) An igneous plagioclase thermometer. *Contributions to Mineralogy and Petrology* 25: 52-65.
- Loomis, T.P. & Welber, P.W. (1982) Crystallization processes in the Rocky Hill granodiorite Pluton, California: An interpretation based on compositional zoning of plagioclase. *Contributions to Mineralogy and Petrology* 81: 230–239.
- Ludwig, K.R. (2009) Squid 2: A user's manual, rev. 12. Berkeley Geochronology Center Special Publication 5: 100.
- Ludwig, K.R. (2012) User's manual for Isoplot 3.75: A geochronological toolkit for Microsoft Excel. *Berkeley Geochronology Center Special Publication* 5: 75.
- Marcaida, M., Vazquez, J.A., Stelten, M.E., Miller, J.S. (2019) Constraining the early eruptive history of the Mono Craters Rhyolites, California, based on ^{238}U - ^{230}Th isochron dating of their explosive and effusive products. *Geochemistry, Geophysics, Geosystems* 20(3): 1539-1556.
- Marsh, B. D. (1988) Crystal size distribution (CSD) in rocks and the kinetics and dynamics of crystallization. *Contributions to Mineralogy and Petrology* 99: 277–291.
- Mason, B. G., Pyle, D. M. & Oppenheimer, C. (2004) The size and frequency of the largest explosive eruptions on Earth. *Bulletin of Volcanology* 66(8): 735–748.
- Mani, L., Tzachor, A. & Cole, P. (2021) Global catastrophic risk from lower magnitude volcanic eruptions. *Nature Communications* 12(1): 4756.

- McCormick, T. C. (1989) Partial homogenization of cryptoperthites in an ignimbrite cooling unit. *Contributions to Mineralogy and Petrology* 101: 104-111.
- Míková, J., & Denková, P. (2012) Modified chromatographic separation scheme for Sr and Nd isotope analysis in geological silicate samples. *Journal of Geosciences* 52: 221–226.
- Ostapenko, G. T., Gamarnik, M. Y., Gorgogotskaya, L. I., Kuznetsov, G. V., Tarashchan, A. N., & Timoshkova, L. P. (1987) Isomorphism of titanium substitution for silicon in quartz: Experimental data. *Mineral Zh* 9, 30–40.
- Ostapenko, G. T., Tarashchan, A. N., & Mitsyuk, B. M. (2007) Rutile-quartz geothermobarometer. *Geochemistry International* 45(5): 506–508.
- Pearce T. H., Kolisnik A. M. (1990) Observations of plagioclase zoning using interference imaging, *Earth-Science Reviews* 29: 9-26.
- Pietranik, A., Koepke, J., & Puziewicz, J. (2006) Crystallization and resorption in plutonic plagioclase: Implications on the evolution of granodiorite magma (Gęsiniec granodiorite, Strzelin Crystalline Massif, SW Poland). *Lithos* 86(3–4): 260–280.
- Putirka, K. (2008) Thermometers and Barometers for Volcanic Systems. In: Putirka, K., Tepley, F. (Eds.), Minerals, Inclusions and Volcanic Processes, *Reviews in Mineralogy and Geochemistry*, Mineralogical Soc. Am. 69: 61-120.
- Randolph A. D., Larson M. A. (1971) Theory of particulate processes. Academic Press, New York, 251 pp.
- Reid, M.R., Coath, C.D., Harrison, T.M., McKeegan, K.D. (1997) Prolonged residence times for the youngest rhyolites associated with Long Valley caldera: Ion microprobe dating of young zircons. *Earth and Planetary Science Letters* 150: 27-38.
- Reid, M. R. (2008) How long does it take to supersize an eruption? *Elements* 4: 23-28.

Schmitt, A. K. (2011) Uranium series accessory crystal dating of magmatic processes.

Annual Review of Earth and Planetary Sciences 39: 321-349.

Self, S., Kircher, D. E., & Wolff, J. A. (1988) The El Cajete Series, Valles Caldera, New

Mexico. *Journal of Geophysical Research* 93(B6): 6113-6127.

Self, S., Wolff, J. A., Spell, T. L., Skuba, C. E., & Morrissey, M. M. (1991) Revisions to the stratigraphy and volcanology of the post-0.5 Ma units and the volcanic section of VC-1

core hole, Valles Caldera, New Mexico. *Journal of Geophysical Research: Solid Earth* 96(B3): 4107–4116.

Siebach, K. L., G. Costin, E. Moreland, and Y. Jiang. (2022) MIST: An Algorithm for

Automating Mineral Identification by Stoichiometry. Int. Mineralogical Assoc. Meeting 2022, OL40_5 (abstract).

Smith, R. L., & Bailey, R. A. (1968) Resurgent Cauldrons. In *Geological Society of America*

Memoirs 116: 613–662.

Spell, T. L., Kyle, P. R., Thirlwall, M. F., & Campbell, A. R. (1993) Isotopic and

geochemical constraints on the origin and evolution of postcollapse rhyolites in the

Valles Caldera, New Mexico. *Journal of Geophysical Research: Solid Earth* 98(B11): 19723–19739.

Tanguy, J.-C., Ribière, C., Scarth, A., & Tjetjep, W. S. (1998) Victims from volcanic

eruptions: A revised database. *Bulletin of Volcanology* 60(2): 137–144.

Tepley, F. J. III, Davidson, J. P. & Clynne, M. A. (1999) Magmatic Interactions as Recorded

in Plagioclase Phenocrysts of Chaos Crags, Lassen Volcanic Center, California, *Journal of Petrology* 40: 787–806.

- Thomas, J. B., Bruce Watson, E., Spear, F. S., Shemella, P. T., Nayak, S. K., & Lanzirotti, A. (2010) TitaniQ under pressure: The effect of pressure and temperature on the solubility of Ti in quartz. *Contributions to Mineralogy and Petrology* 160(5): 743–759.
- Tsuchiyama A. (1985) Dissolution kinetics of plagioclase in the melt of the system diopside–albite–anorthite, and the origin of dusty plagioclase in andesites, *Contributions to Mineralogy and Petrology* 89: 1-16.
- Ubide, T., Caulfield, J., Brandt, C., Bussweiler, Y., Mollo, S., Di Stefano, F., Nazzari, M., & Scarlato, P. (2019) Deep Magma Storage Revealed by Multi-Method Elemental Mapping of Clinopyroxene Megacrysts at Stromboli Volcano. *Frontiers in Earth Science* 7: 239.
- Vazquez, J.A., Lidzbarski, M.I. (2012) High-resolution tephrochronology of the Wilson Creek Formation (Mono Lake, California) and Laschamp event using ^{238}U - ^{230}Th SIMS dating of accessory mineral rims. *Earth and Planetary Science Letters* 357-358: 54-67.
- Wark, D. A., & Watson, E. B. (2006) TitaniQ: A titanium-in-quartz geothermometer. *Contributions to Mineralogy and Petrology* 152(6): 743–754.
- Watson, E.B., Harrison, T.M. (2005) Zircon thermometer reveals minimum melting conditions on earliest Earth. *Science* 308: 841-844.
- Westgate, J.A., WoldeGabriel, G., Halls, H.C., Bray, C.J., Barendregt, R.W., Pearce, N.J.G., Sarna-Wojcicki, A.M., Gorton, M.P., Kelley, R.E., Schultz-Fellenz, E. (2018) Quaternary tephra from the Valles caldera in the volcanic field of the Jemez Mountains of New Mexico identified in western Canada. *Quaternary Research* 91(2): 813-828.
- Wolff, J. A., Gardner, J. N. (1995) Is the Valles caldera entering a new cycle of activity? *Geology* 23(5): 411-414.

- Wolff, J. A., Brunstad, K. A., Gardner, J. N. (2011) Reconstruction of the most recent volcanic eruptions from the Valles caldera, New Mexico. *Journal of Volcanology and Geothermal Research* 199(1–2): 53–68.
- Wolff, J. A., Neukampf, J. (2022) Biotite as an indicator of post-eruptive cryptic alteration in the Battleship Rock Ignimbrite, Valles Caldera, NM, USA. *Bulletin of Volcanology* 84: 99.
- Zimmerer, M. J., Lafferty, J., Coble, M. A. (2016) The eruptive and magmatic history of the youngest pulse of volcanism at the Valles caldera: Implications for successfully dating late Quaternary eruptions. *Journal of Volcanology and Geothermal Research*, 310: 50–57.
- Zou, H. B. (1999). *Studies of mantle melting process and compositions using major and trace elements, neodymium-strontium-lead isotopic systematics, and uranium series disequilibria: Mathematical modeling and experimental analyses*. Florida State University, 185pp.
- Zou, H.B., Fan, Q.C., Schmitt, A.K., Sui, J.L. (2010a) U-Th dating of zircons from Holocene potassic andesites (Maanshan volcano, Tengchong, SE Tibetan Plateau) by depth profiling: Time scales and nature of magma storage. *Lithos* 118: 202–210.
- Zou, H.B., Fan, Q.C., Zhang, H.F. (2010b) Rapid development of the great Millennium eruption of Changbaishan (Tianchi) Volcano: Evidence from U-Th zircon dating. *Lithos* 119: 289-296.
- Zou, H.B., Vazquez, J.A., Zhao, Y.W., Guo, Z.P. (2021) Zircon surface crystallization ages for the extremely reduced magmatic products of the Millennium Eruption, Changbaishan Volcano (China/North Korea). *Gondwana Research* 92: 172-183.

Appendix 1: EMPA Data

BSH16-1	SiO2	Al2O3	FeO	MnO	MgO	CaO	Na2O	K2O	Total	Min ID
1	15.14	1.254	0.285	0	0.124	0.332	0.485	0.807	18.428	Framework Silicate
2	42.55	8.03	14.26	0.077	11.99	11.44	1.8	0.642	90.789	Calcic Amphibole
3	51.82	0.61	8.99	0.026	16.11	20.78	0.191	0.005	98.532	Augite
4	52.73	0.42	8.34	0	16.52	20.86	0.234	0.008	99.112	Augite
5	50.92	0.508	8.12	0.026	16.08	20.18	0.331	0.02	96.185	Augite
6	72.36	13.02	0.478	0.141	0.205	0.98	2.66	4.51	94.354	Clinoptilolite-K
7	57.96	10.9	0.609	0.064	0.319	0.826	1.911	3.73	76.318	Clinoptilolite-K
8	71.78	13.41	0.861	0.141	0.277	1.134	2.883	4.45	94.934	Clinoptilolite-K
9	72.77	13.55	1.144	0	0.235	1.165	2.701	4.35	95.915	Clinoptilolite-K
10	48.77	6.2	10.94	0.229	17.75	10.77	1.252	0.6	96.51	Calcic Amphibole
11	62.22	12.1	4.87	0	5.67	4.4	2.345	2.889	94.494	Amph-Px
12	47.73	8.04	11.52	0.078	16.44	10.82	1.7	0.642	96.97	Calcic Amphibole
13	52.84	10.34	9.02	0.183	12.39	8.32	1.925	1.404	96.423	Amphibole
14	15.18	1.188	0.521	0.067	0.172	0.322	0.624	0.755	18.829	Framework Silicate
15	46.5	8.24	11.76	0	16.23	10.7	1.802	0.668	95.901	Calcic Amphibole
16	75.28	13.87	1.067	0	0.326	1.141	2.752	4.39	98.826	Clinoptilolite-K
17	68.33	12.6	1.022	0.179	0.169	1.099	2.284	4.1	89.783	Clinoptilolite-K
18	74.8	14.05	1.294	0.069	0.291	1.132	2.967	4.35	98.952	Clinoptilolite-Na
19	73.77	13.88	1.159	0.028	0.265	1.15	2.808	4.35	97.41	Clinoptilolite-K
20	44.97	6.82	11.9	0	14.47	9.95	1.271	0.599	89.98	Calcic Amphibole
21	48.77	7.76	11.96	0.169	16.7	10.6	1.658	0.59	98.207	Calcic Amphibole
22	47.83	8.32	11.84	0	16.01	10.73	1.831	0.604	97.165	Calcic Amphibole
23	50.33	6.61	12.18	0	17.36	10.77	1.124	0.584	98.958	Calcic Amphibole
24	74.45	13.28	0.863	0	0.154	1.072	2.915	4.21	96.944	Clinoptilolite-Na
25	75.92	13.77	0.9	0.206	0.246	1.03	2.987	4.26	99.319	Clinoptilolite-Na
26	65.86	11.64	0.413	0.193	0.184	0.854	1.714	3.59	84.448	Framework Silicate

BSH16-2	SiO2	Al2O3	FeO	MnO	MgO	CaO	Na2O	K2O	Total	Min ID
1	72.3	13.1	0.511	0.302	0.308	0.965	2.623	4.89	94.999	Clinoptilolite-K
2	53.7	0.847	17.82	0.037	27.37	1.163	0	0	100.937	Orthopyroxene
3	53.87	0.496	17.09	0	28.04	1.008	0.124	0	100.628	Orthopyroxene
4	53.63	6.13	9.56	0	13.34	0.895	0.712	1.737	86.004	Amph-Px
5	53.83	0.877	17.93	0	28.46	0.959	0	0.005	102.06	Pyroxene
6	72.34	13.91	0.299	0.198	0.027	0.629	3.13	4.81	95.342	Clinoptilolite-K
7	74.16	13.89	0.322	0	0.086	0.641	2.704	4.8	96.602	Clinoptilolite-K
8	75.95	13.15	0.295	0	0.106	0.511	2.708	4.74	97.46	Clinoptilolite-K
9	49.12	5.39	11.07	0.278	17.83	10.89	1.241	0.533	96.353	Calcic Amphibole
10	54.92	8.8	8.13	0	12.38	7.57	1.834	1.658	95.292	Amphibole
11	0.008	1.736	82.34	0.096	1.728	0.046	0	0.009	85.963	amakinite or wustite
12	0	1.846	81.6	0.022	1.664	0.06	0	0.008	85.2	amakinite or wustite
13	0.004	1.857	83.61	0.132	1.677	0.055	0.047	0.012	87.395	amakinite or wustite
14	54.68	0.821	17.61	0.268	26.09	1.043	0	0.022	100.535	Orthopyroxene
15	67.2	18.2	0.24	0.381	0.037	3.6	4.34	3.04	97.038	Heulandite-Na
16	53.3	0.757	8.7	0.324	15.89	20.05	0.339	0	99.36	Augite
17	52.91	0.793	8.66	0.113	15.3	19.59	0.368	0.017	97.751	Augite
18	52.87	0.737	7.7	0.412	15.79	20.24	0.254	0	98.003	Augite
19	74.64	12.09	0.993	0.158	0.107	0.309	2.431	5.14	95.867	Clinoptilolite-K
20	74.93	12.33	1.055	0.444	0.085	0.307	2.391	5.07	96.613	Clinoptilolite-K
21	75.84	12.63	0.961	0.187	0.076	0.338	2.468	5.14	97.64	Clinoptilolite-K
22	75.93	14.17	1.064	0.051	0.199	0.972	2.73	4.53	99.645	Clinoptilolite-K
23	104.24	0.03	0.057	0.052	0.005	0.012	0	0	104.396	Quartz
24	74.46	13.54	1.084	0	0.013	0.743	2.879	4.92	97.639	Clinoptilolite-K
25	74.46	13.5	1.18	0.382	0.256	0.834	2.571	4.7	97.883	Clinoptilolite-K
26	73.79	13.15	1.159	0.217	0.258	0.905	2.875	4.72	97.073	Clinoptilolite-K
27	55.95	27.62	0.32	0	0.025	9.73	5.76	0.41	99.815	Plagioclase
28	4.77	0.7	0.048	0.049	0.027	0.421	0.118	0.262	6.395	Clinoptilolite-Ca
29	57.21	27.6	0.226	0.231	0	8.9	6.17	0.424	100.761	Plagioclase
30	58.08	27.74	0.211	0	0.005	8.87	6.26	0.433	101.599	Plagioclase
31	57.56	27.18	0.248	0	0	9.03	5.88	0.44	100.338	Plagioclase
32	55.42	27.49	0.274	0	0.032	9.81	5.09	0.385	98.501	Plagioclase
33	0	0	0.139	0	0.114	53.02	0	0.02	53.293	calcite
34	62.83	24.78	0.272	0.992	0.024	6.82	7.24	0.689	103.648	Plagioclase
35	61.66	23.64	0.297	0	0.038	6.14	7.23	0.739	99.744	Plagioclase
36	55.59	28.48	0.391	0.102	0.008	10.9	5.46	0.321	101.252	Plagioclase
37	54.97	28.7	0.374	0.177	0.06	10.76	5.24	0.305	100.586	Plagioclase
38	64.11	21.97	0.565	0.075	0.096	7.29	4.2	2.026	100.331	Plagioclase
39	63.07	23.27	0.594	0.199	0.091	6.7	5.71	1.337	100.972	Plagioclase
40	57.43	26.12	0.387	0	0.022	8.83	6.28	0.419	99.488	Plagioclase
41	56.3	28.31	0.267	0.47	0.004	10.28	5.62	0.324	101.575	Plagioclase
42	55.91	28	0.268	0.398	0.021	10.47	5.35	0.37	100.786	Plagioclase
43	58.35	26.32	0.487	0.128	0.047	8.75	5.77	0.411	100.262	Plagioclase
44	59.85	25.83	0.388	0.078	0.021	6.86	7.1	0.712	100.839	Plagioclase
45	68.58	20.03	0.71	0.079	0.046	4.51	4.25	2.888	101.092	Heulandite-Na
46	68.06	12.37	3.77	0.013	0.258	0.842	2.535	4.17	92.017	Silicate
47	60.21	26.45	0.54	0.345	0.017	9.47	4.35	1.056	102.439	Plagioclase
48	55.51	29.69	0.438	0.199	0.042	10.96	5.31	0.298	102.446	Plagioclase
49	70.92	16.82	0.795	0.133	0.212	2.647	4.04	3.86	99.427	Heulandite-Na
50	54.46	30.2	0.301	0.16	0.023	11.04	4.85	0.283	101.317	Plagioclase
51	55.24	30.02	0.323	0.108	0.002	10.89	5.25	0.298	102.132	Plagioclase
52	54.89	29.24	0.609	0.121	0.002	10.57	4.92	0.293	100.645	Plagioclase
53	74.74	13.73	1.129	0.068	0.13	0.789	2.819	4.97	98.374	Clinoptilolite-K

BSH16-3	SiO2	Al2O3	FeO	MnO	MgO	CaO	Na2O	K2O	Total	Min ID
1	63.66	21.67	0.667	0.053	0.153	6.39	4.35	2.058	99.001	Plagioclase
2	54.75	27.73	0.33	0	0.024	10.54	4.86	0.399	98.633	Plagioclase
3	74.79	12.46	1.002	0	0.333	0.644	2.414	4.95	96.593	Clinoptilolite-K
4	0.46	0.034	0	0.013	0.03	0.051	0	0.006	0.593	Silicate
5	54.36	27.84	0.291	0	0.019	10.11	5.17	0.296	98.085	Plagioclase
6	66.38	19.36	0.814	0.013	0.184	4.49	4.01	2.677	97.927	Heulandite-Na
7	54.52	27.94	0.374	0.051	0	10.12	4.65	0.33	97.985	Plagioclase
8	71.77	13.46	0.358	0.18	0.053	0.492	2.549	5.41	94.272	Clinoptilolite-K
9	58.94	23.72	0.224	0	0.034	6.08	6.48	0.767	96.245	Plagioclase
10	66.72	8.61	0.447	0	0.36	1.204	2.953	1.168	81.461	Framework Silicate
11	66.29	10.43	0.431	0.167	0.28	0.493	1.979	3.95	84.021	Framework Silicate
12	65.34	12.83	0.374	0.013	0.056	0.865	2.215	4.35	86.043	Clinoptilolite-K
13	52.77	28.67	0.515	0.026	0.064	11.13	4.32	0.295	97.79	Plagioclase
14	73.74	12.88	1.278	0.154	0.437	0.704	2.614	5.2	97.007	Clinoptilolite-K
15	54.53	28.35	0.4	0.052	0.002	10.51	4.94	0.351	99.134	Plagioclase
16	75.06	13.13	1.092	0.039	0.253	0.715	2.416	5.32	98.026	Clinoptilolite-K
17	55.32	28.72	0.383	0.051	0.029	9.91	5.01	0.387	99.809	Plagioclase
18	70.1	13.69	0.272	0.142	0.018	0.555	2.62	5.36	92.756	Clinoptilolite-K
19	57.96	24.57	0.275	0	0.053	6.36	6.61	0.714	96.541	Plagioclase
20	54.99	26.08	0.415	0	0.048	8.89	5.57	0.405	96.397	Plagioclase
21	51.83	27	0.37	0	0	10.18	4.91	0.331	94.621	Plagioclase
22	52.19	27.56	0.317	0.026	0.041	10.38	4.72	0.287	95.519	Plagioclase
23	56.35	25.25	0.418	0	0.056	8.52	5.08	0.645	96.318	Plagioclase
24	5.37	1.179	0.423	0	0.377	0.135	0.209	0.264	7.957	Amph-Px
25	65.47	17.54	0.704	0.078	0.192	3.81	3.9	3.24	94.934	Heulandite-Na
26	54.95	26.39	0.301	0.129	0.014	8.95	5.49	0.43	96.653	Plagioclase
27	60.57	20.56	0.684	0.168	0.159	5.81	4.17	2.191	94.313	Plagioclase
28	71.3	12.82	1.383	0.234	0.418	0.627	2.58	5.21	94.57	Clinoptilolite-K
29	71.93	12.94	1.272	0.233	0.333	0.656	2.653	5.21	95.227	Clinoptilolite-K
30	59.56	23.27	0.51	0.117	0.093	7.15	4.42	1.398	96.518	Montmorillonite
31	63.25	11.99	1.216	0.169	0.285	1.107	2.25	4.78	85.047	Clinoptilolite-K
32	52.97	27.99	0.295	0	0.012	9.93	5.04	0.298	96.536	Plagioclase
33	55.82	27.49	0.391	0.079	0.033	8.6	5.74	0.421	98.574	Plagioclase
34	51.37	26.59	0.317	0.117	0.036	8.79	5.42	0.399	93.039	Plagioclase
35	70.14	13.09	1.267	0	0.383	0.871	2.686	4.92	93.357	Clinoptilolite-K
36	63.91	12.18	0.304	0.092	0.068	0.718	1.944	4.68	83.896	Clinoptilolite-K
37	69.57	14.06	0.717	0.351	0.081	1.196	3.03	4.83	93.835	Clinoptilolite-K
38	52.79	27.7	0.225	0.092	0.045	9.6	5.02	0.356	95.828	Plagioclase
39	58.6	23.04	0.523	0.039	0.11	6.55	5.08	1.418	95.361	Plagioclase
40	58.17	23.28	0.526	0	0.063	6.69	5.11	1.24	95.079	Plagioclase
41	52.3	28.17	0.304	0	0.019	10.13	4.84	0.346	96.109	Plagioclase
42	53.47	26.42	0.23	0.079	0.014	8.28	5.86	0.492	94.845	Plagioclase
43	70.52	12.84	1.326	0.144	0.376	0.739	2.527	5.28	93.752	Clinoptilolite-K
44	50.44	26.25	0.362	0	0.038	9.27	4.86	0.387	91.608	Plagioclase
45	51.13	28.66	0.406	0.105	0.057	10.79	4.45	0.267	95.865	Plagioclase
46	60.24	21.04	0.723	0.131	0.064	5.67	4.72	2.114	94.702	Plagioclase
47	54.94	25.68	0.321	0	0.009	7.29	6.22	0.428	94.888	Plagioclase
48	54.78	26.24	0.31	0	0	8.41	5.91	0.403	96.053	Plagioclase
49	40.83	17.76	0.219	0.248	0.031	4.87	4.85	0.255	69.063	Plagioclase
50	53.99	6.39	0.542	0.105	1.069	0.763	1.683	1.17	65.711	Framework Silicate
51	56.48	9.66	0.234	0.105	0.1	1.002	2.959	1.788	72.328	Clinoptilolite-Na
52	50.54	0.933	7.82	0	15.5	19.01	0.282	0.062	94.146	Augite

53	70.24	12.9	1.427	0	0.104	0.363	2.383	5.46	92.877	Clinoptilolite-K
54	50.97	0.499	8.42	0.027	16.32	19.35	0.304	0	95.89	Augite
55	70.61	13.36	0.21	0.176	0.068	0.388	2.373	5.51	92.695	Clinoptilolite-K
56	55.95	12.88	0.584	0.15	0.127	1.394	3.34	2.217	76.641	Heulandite-Na
57	70.52	12.99	0.207	0.041	0.049	0.359	2.656	5.44	92.261	Clinoptilolite-K
58	51.3	0.471	8.13	0.041	16.23	19.42	0.289	0.004	95.885	Augite
59	52.54	0.55	8.03	0	16.06	18.05	0.395	0.024	95.648	Augite
60	38.48	1.158	6.65	0	9.27	14.76	1.106	0.166	71.59	Amph-Px
61	89.28	3.44	0.15	0	0.026	0.074	0.892	1.68	95.542	SiO2 Phase
62	31.7	16.64	29.87	0.173	3.09	0	0.222	8.98	90.676	Biotite (Annite)
63	45.57	6.43	11.42	0	16.35	10.03	1.39	0.579	91.769	Calcic Amphibole
64	70.45	12.28	0.217	0	0.08	0.688	2.54	4.92	91.175	Clinoptilolite-K
65	71.77	12.55	0.302	0.28	0.126	0.632	2.545	5.24	93.445	Clinoptilolite-K
66	42.89	5.73	9.94	0.041	15.45	12.7	1.541	0.576	88.868	Calcic Amphibole
67	45.38	7.95	11.52	0.055	16.32	10.16	1.639	0.541	93.566	Calcic Amphibole
68	58.29	10.81	17.12	0	0.862	0.648	2.433	4.01	94.173	Amph-Px
69	72.49	13.27	0.39	0.157	0.121	0.717	2.478	5.1	94.723	Clinoptilolite-K
70	72.39	13.04	0.336	0.3	0.098	0.723	2.652	5.1	94.639	Clinoptilolite-K
71	70.62	13.03	0.757	0.513	0.067	0.773	2.647	5.02	93.426	Clinoptilolite-K
72	44.65	6.54	11.23	0.21	14.8	9.81	1.434	0.608	89.282	Calcic Amphibole
73	51.46	8.5	9.54	0	13.35	8.57	1.708	1.449	94.577	Amphibole
74	46.62	6.49	11.58	0	16.42	10.25	1.185	0.57	93.115	Calcic Amphibole
75	46.34	6.9	11.42	0.127	16.13	10.1	1.331	0.61	92.958	Calcic Amphibole
76	45.79	7.01	11.29	0	16.19	10.18	1.513	0.596	92.569	Calcic Amphibole
77	67.16	12.47	1.355	0.129	0.331	0.845	2.288	4.7	89.278	Clinoptilolite-K
78	72.55	13.4	0.507	0.058	0.105	0.819	2.34	4.99	94.769	Clinoptilolite-K

APPENDIX 2: Plagioclase Thermometry Data

Sample	WR (Self et al.)	BSH16-2									
		1	2	3	4	5	6	7	8	9	10
SiO ₂	73.28	57.21	58.08	57.56	55.42	62.83	61.66	55.59	54.97	64.11	63.07
TiO ₂	0.29	-	-	-	-	-	-	-	-	-	-
Al ₂ O ₃	13.52	27.60	27.74	27.18	27.49	24.78	23.64	28.48	28.70	21.97	23.27
FeO	2.10	0.23	0.21	0.25	0.27	0.27	0.30	0.39	0.37	0.57	0.59
MnO	0.05	0.23	0.00	0.00	0.00	0.99	0.00	0.10	0.18	0.08	0.20
MgO	0.86	0.00	0.01	0.00	0.03	0.02	0.04	0.01	0.06	0.10	0.09
CaO	1.63	8.90	8.87	9.03	9.81	6.82	6.14	10.90	10.76	7.29	6.70
Na ₂ O	3.99	6.17	6.26	5.88	5.09	7.24	7.23	5.46	5.24	4.20	5.71
K ₂ O	4.19	0.42	0.43	0.44	0.39	0.69	0.74	0.32	0.31	2.03	1.34
Cr ₂ O ₃	0.12	-	-	-	-	-	-	-	-	-	-
P ₂ O ₅	0.08	-	-	-	-	-	-	-	-	-	-
H ₂ O	3.80	-	-	-	-	-	-	-	-	-	-
T (C)		1035.8	1035.3	1037.9	1031.2	1013.8	1003.9	1023.0	1023.7	1016.1	999.8
K _D (Ab-An)		0.06	0.06	0.06	0.05	0.09	0.10	0.04	0.04	0.05	0.08

		BSH16-2																		
Sample	WR (Self et al.)	11	12	13	14	15	16	17	18	19	20									
SiO ₂	73.28	57.43	56.30	55.91	58.35	59.85	60.21	55.51	54.46	55.24	54.89									
TiO ₂	0.29	-	-	-	-	-	-	-	-	-	-									
Al ₂ O ₃	13.52	26.12	28.31	28.00	26.32	25.83	26.45	29.69	30.2	30.02	29.24									
FeO	2.10	0.39	0.27	0.27	0.49	0.39	0.54	0.438	0.301	0.323	0.609									
MnO	0.05	0.00	0.47	0.40	0.13	0.08	0.345	0.199	0.16	0.108	0.121									
MgO	0.86	0.02	0.00	0.02	0.05	0.02	0.017	0.042	0.023	0.002	0.002									
CaO	1.63	8.83	10.28	10.47	8.75	6.86	9.47	10.96	11.04	10.89	10.57									
Na ₂ O	3.99	6.28	5.62	5.35	5.77	7.10	4.35	5.31	4.85	5.25	4.92									
K ₂ O	4.19	0.42	0.32	0.37	0.41	0.71	1.056	0.298	0.283	0.298	0.293									
Cr ₂ O ₃	0.12	-	-	-	-	-	-	-	-	-	-									
P ₂ O ₅	0.08	-	-	-	-	-	-	-	-	-	-									
H ₂ O	3.80	-	-	-	-	-	-	-	-	-	-									
T (C)		993.9	1000.4	1030.5	1023.9	1003.9	1028.6	1020.8	1023.2	1021.0	1015.7									
K _p (Ab-An)		0.06	0.05	0.05	0.06	0.09	0.04	0.04	0.04	0.04	0.04									

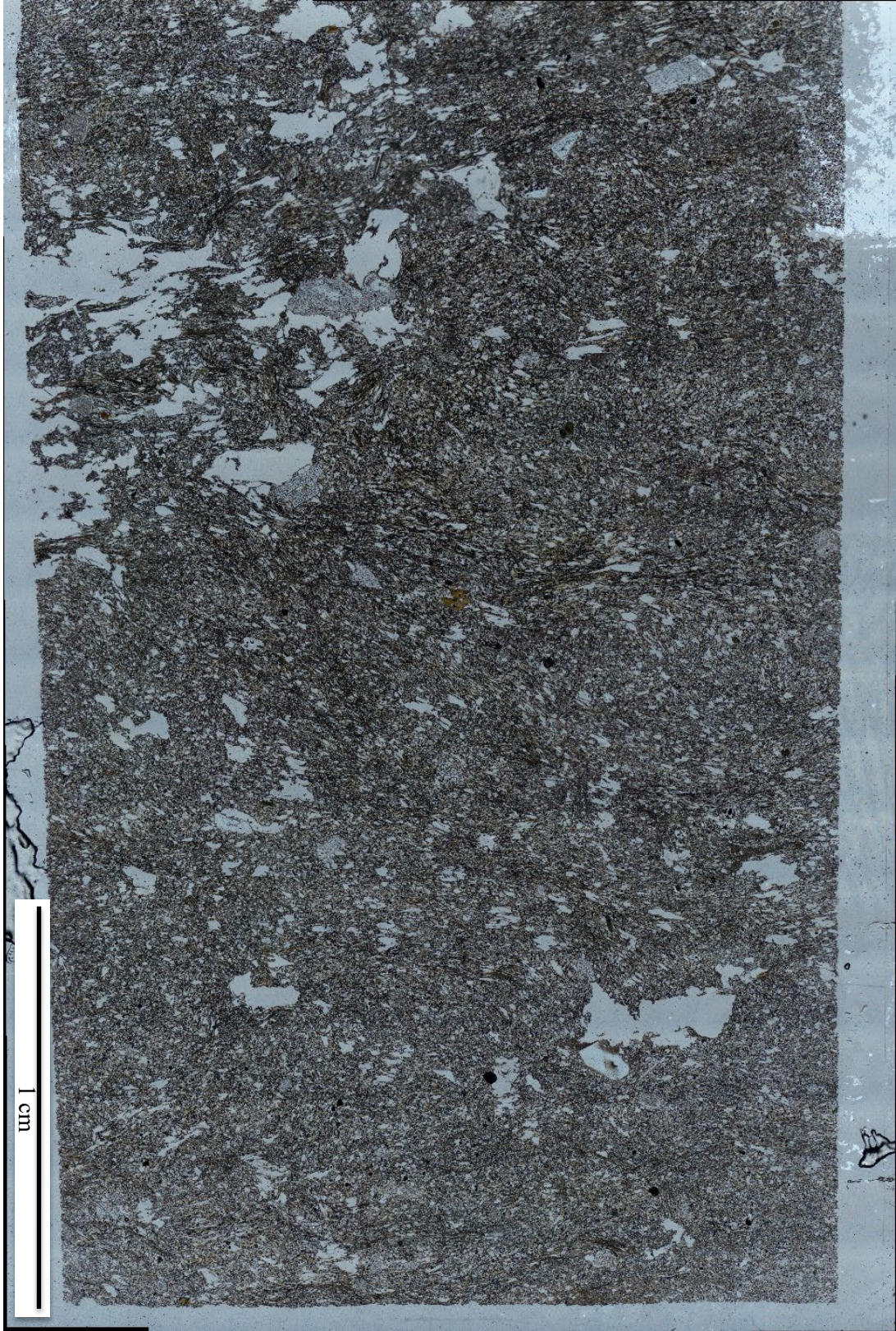
		BSH16-3									
Sample	WR (Self et al.)	1	2	3	4	5	6	7	8	9	10
SiO ₂	73.28	63.66	54.75	54.36	54.52	58.94	52.77	54.53	55.32	57.96	54.99
TiO ₂	0.29	-	-	-	-	-	-	-	-	-	-
Al ₂ O ₃	13.52	21.67	27.73	27.84	27.94	23.72	28.67	28.35	28.72	24.57	26.08
FeO	2.10	0.667	0.33	0.291	0.374	0.224	0.515	0.4	0.383	0.275	0.415
MnO	0.05	0.053	0	0	0.051	0	0.026	0.052	0.051	0	0
MgO	0.86	0.153	0.024	0.019	0	0.034	0.064	0.002	0.029	0.053	0.048
CaO	1.63	6.39	10.54	10.11	10.12	6.08	11.13	10.51	9.91	6.36	8.89
Na ₂ O	3.99	4.35	4.86	5.17	4.65	6.48	4.32	4.94	5.01	6.61	5.57
K ₂ O	4.19	2.058	0.399	0.296	0.33	0.767	0.295	0.351	0.387	0.714	0.405
Cr ₂ O ₃	0.12	-	-	-	-	-	-	-	-	-	-
P ₂ O ₅	0.08	-	-	-	-	-	-	-	-	-	-
H ₂ O	3.80	-	-	-	-	-	-	-	-	-	-
T (C)		1056.7	1047.1	1043.6	1034.0	1015.7	1029.2	1025.0	1023.5	987.3	997.6
K_D (Ab-An)		0.06	0.04	0.05	0.04	0.09	0.03	0.04	0.04	0.09	0.06

		BSH16-3																		
Sample	WR (Self et al.)	11	12	13	14	15	16	17	18	19	20									
SiO ₂	73.28	51.83	52.19	56.35	54.95	60.57	52.97	55.82	51.37	52.79	58.6									
TiO ₂	0.29	-	-	-	-	-	-	-	-	-	-									
Al ₂ O ₃	13.52	27	27.56	25.25	26.39	20.56	27.99	27.49	26.59	27.7	23.04									
FeO	2.10	0.37	0.317	0.418	0.301	0.684	0.295	0.391	0.317	0.225	0.523									
MnO	0.05	0	0.026	0	0.129	0.168	0	0.079	0.117	0.092	0.039									
MgO	0.86	0	0.041	0.056	0.014	0.159	0.012	0.033	0.036	0.045	0.11									
CaO	1.63	10.18	10.38	8.52	8.95	5.81	9.93	8.6	8.79	9.6	6.55									
Na ₂ O	3.99	4.91	4.72	5.08	5.49	4.17	5.04	5.74	5.42	5.02	5.08									
K ₂ O	4.19	0.331	0.287	0.645	0.43	2.191	0.298	0.421	0.399	0.356	1.418									
Cr ₂ O ₃	0.12	-	-	-	-	-	-	-	-	-	-									
P ₂ O ₅	0.08	-	-	-	-	-	-	-	-	-	-									
H ₂ O	3.80	-	-	-	-	-	-	-	-	-	-									
T (C)		1003.8	1004.9	1029.3	1026.2	1034.1	1019.8	1013.4	1015.5	1019.6	1015.2									
K_p (Ab-An)		0.04	0.04	0.05	0.05	0.06	0.05	0.06	0.05	0.05	0.07									

		BSH16-3												
Sample	WR (Self et al.)	21	22	23	24	25	26	27	28	29				
SiO ₂	73.28	58.17	52.3	53.47	50.44	51.13	60.24	54.94	54.78	40.83				
TiO ₂	0.29	-	-	-	-	-	-	-	-	-				
Al ₂ O ₃	13.52	23.28	28.17	26.42	26.25	28.66	21.04	25.68	26.24	17.76				
FeO	2.10	0.526	0.304	0.23	0.362	0.406	0.723	0.321	0.31	0.219				
MnO	0.05	0	0	0.079	0	0.105	0.131	0	0	0.248				
MgO	0.86	0.063	0.019	0.014	0.038	0.057	0.064	0.009	0	0.031				
CaO	1.63	6.69	10.13	8.28	9.27	10.79	5.67	7.29	8.41	4.87				
Na ₂ O	3.99	5.11	4.84	5.86	4.86	4.45	4.72	6.22	5.91	4.85				
K ₂ O	4.19	1.24	0.346	0.492	0.387	0.267	2.114	0.428	0.403	0.255				
Cr ₂ O ₃	0.12	-	-	-	-	-	-	-	-	-				
P ₂ O ₅	0.08	-	-	-	-	-	-	-	-	-				
H ₂ O	3.80	-	-	-	-	-	-	-	-	-				
T (C)		1013.5	1015.6	1006.3	1013.7	1016.2	1019.1	994.2	1000.9	995.0				
K_D (Ab-An)		0.07	0.04	0.06	0.05	0.04	0.07	0.08	0.06	0.90				

Appendix 3: BSH16 Thin-Section Images

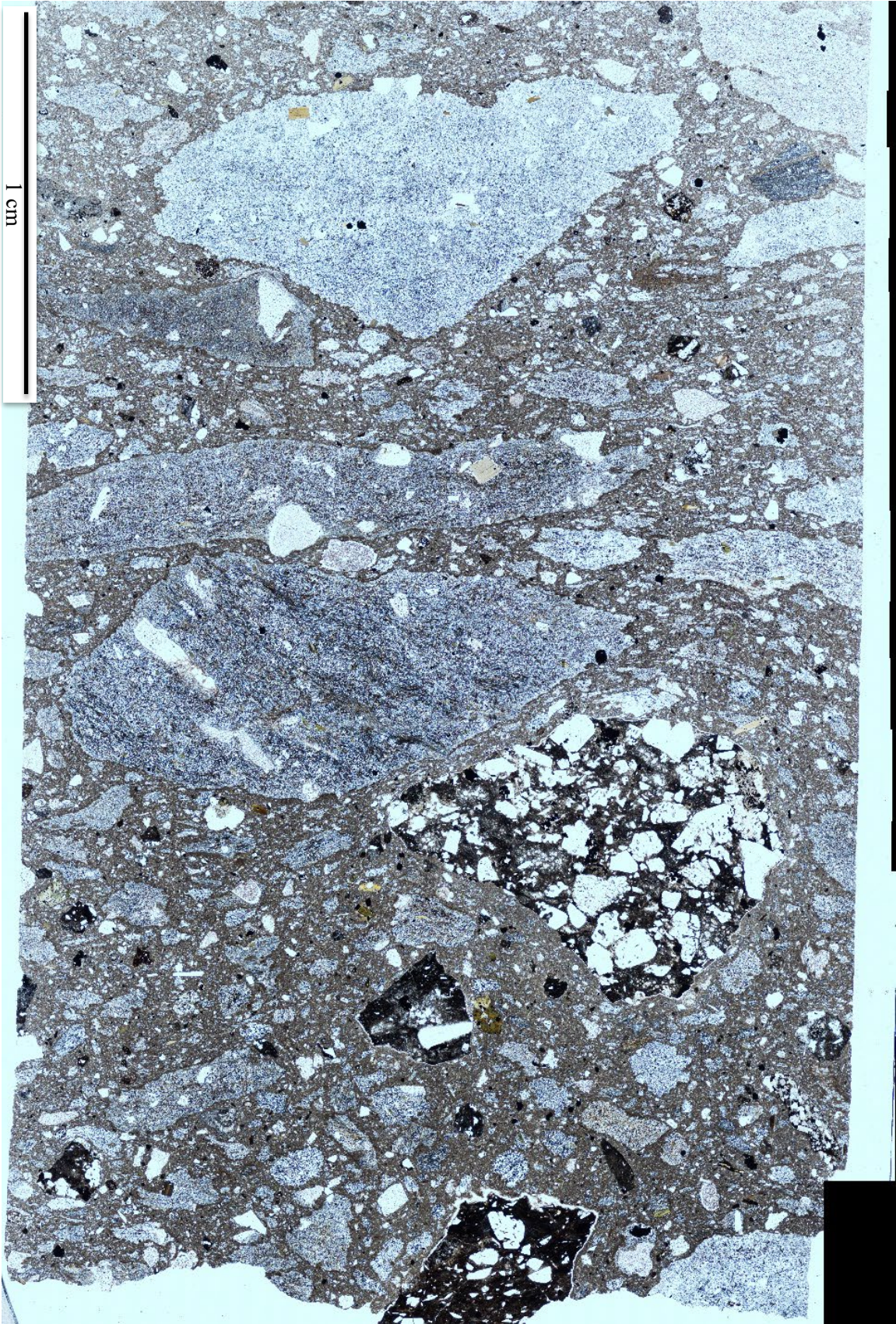
Notes: The following images are composites that were made to facilitate collecting data for the CSD analysis of this study. They are photomicrograph images taken in plain polarized light and stitched together using computer software (in this case, NIS Elements). Each thin section is approximately 3.3 cm by 2 cm in size. The purpose of making these images is so that individual grains can be found, traced (which is done by hand in Adobe Illustrator), and their dimensions used in the CSDCorrections software which returns the CSD analysis results. Ensuring that these images are made with care is paramount to a successful CSD analysis, as any artificial deformation in the image will result in compounding error in the resultant calculations.



BSH16-1 MAP



BSH16-2 MAP



BSH16-3 MAP